

**First-principles study of dehydration interfaces between diaspore and corundum, gibbsite and boehmite, and boehmite and  $\gamma\text{-Al}_2\text{O}_3$   
Energetic stability, interface charge effects, and dehydration defects**

van Gog, Heleen

**DOI**

[10.1016/j.apsusc.2020.148501](https://doi.org/10.1016/j.apsusc.2020.148501)

**Publication date**

2021

**Document Version**

Final published version

**Published in**

Applied Surface Science

**Citation (APA)**

van Gog, H. (2021). First-principles study of dehydration interfaces between diaspore and corundum, gibbsite and boehmite, and boehmite and  $\gamma\text{-Al}_2\text{O}_3$ : Energetic stability, interface charge effects, and dehydration defects. *Applied Surface Science*, 2541, Article 148501.  
<https://doi.org/10.1016/j.apsusc.2020.148501>

**Important note**

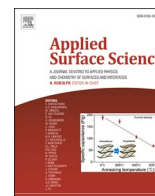
To cite this publication, please use the final published version (if applicable).  
Please check the document version above.

**Copyright**

Other than for strictly personal use, it is not permitted to download, forward or distribute the text or part of it, without the consent of the author(s) and/or copyright holder(s), unless the work is under an open content license such as Creative Commons.

**Takedown policy**

Please contact us and provide details if you believe this document breaches copyrights.  
We will remove access to the work immediately and investigate your claim.



## Full Length Article

# First-principles study of dehydration interfaces between diaspore and corundum, gibbsite and boehmite, and boehmite and $\gamma$ -Al<sub>2</sub>O<sub>3</sub>: Energetic stability, interface charge effects, and dehydration defects

Heleen van Gog

Engineering Thermodynamics, Process & Energy Department, Faculty of Mechanical, Maritime and Materials Engineering, Delft University of Technology, Leeghwaterstraat 39, 2628 CB Delft, the Netherlands



## ARTICLE INFO

## Keywords:

Alumina  
Aluminum hydrates  
Density functional theory  
Interfaces  
Dehydration

## ABSTRACT

Aluminum hydrate dehydration interfaces were studied using a van der Waals density functional. The interface configurations investigated here as a first exploration of possible interface geometries, were all found to have a reasonable probability of occurring. From gibbsite/boehmite and boehmite/ $\gamma$ -Al<sub>2</sub>O<sub>3</sub> interface simulation cells, the formation of dehydration-related defects during relaxation was observed. H transfer between hydroxyl groups, and separation of hydroxyl groups and H atoms from the lattice, resulted in the formation of chemisorbed H<sub>2</sub>O and OH<sub>2</sub> groups in gibbsite; in boehmite, the formation of OH<sub>2</sub> groups and interstitial H was observed. All interfaces show a transfer of small amounts of charge across the interface. Accumulation of charge in spaces interstitial to the lattice was found to play a role in the dehydration process as well. The present study shows the potential of interface studies for elucidating dehydration pathways at the atomic scale, and offers various starting-points for follow-up studies.

## 1. Introduction

Alumina (Al<sub>2</sub>O<sub>3</sub>) is a ceramic material of high industrial and technological importance. Besides the thermodynamically stable corundum form ( $\alpha$ -Al<sub>2</sub>O<sub>3</sub>), many metastable polymorphs exist. These so-called transition aluminas are stable at ambient conditions, and are designated as  $\gamma$ -,  $\kappa$ -,  $\theta$ -,  $\gamma$ -,  $\delta$ -,  $\eta$ -, and  $\rho$ -Al<sub>2</sub>O<sub>3</sub> (see Fig. 1) [1–3].  $\alpha$ -Al<sub>2</sub>O<sub>3</sub> is mainly seen as a structural, optical, and electronic material.  $\gamma$ -Al<sub>2</sub>O<sub>3</sub> is the most investigated transition alumina, and has a most prominent application as catalyst and catalytic support. In nanocrystalline form,  $\gamma$ -Al<sub>2</sub>O<sub>3</sub> is more stable than  $\alpha$ -Al<sub>2</sub>O<sub>3</sub>; the lower surface energy of the former thermodynamically stabilizes nanoscale  $\gamma$ -Al<sub>2</sub>O<sub>3</sub> over nanoscale  $\alpha$ -Al<sub>2</sub>O<sub>3</sub>, as was shown by McHale et al. [4]. An example of a most promising application of nanoscale alumina is the use of Al<sub>2</sub>O<sub>3</sub> nanosheets and Al<sub>2</sub>O<sub>3</sub> nanoribbons in nanoelectronics, which in studies by Liao et al. [5], Chae et al. [6], and Jung et al. [7], was found to be a most exciting progression towards the realization of high-performance graphene-based field effect transistors.

Aluminum hydroxides are the hydrated precursors of the alumina phases. There are seven different known aluminum hydroxides: the four trihydroxide polymorphs gibbsite ( $\gamma$ -Al(OH)<sub>3</sub>), bayerite ( $\alpha$ -Al(OH)<sub>3</sub>), nordstrandite, and doyleite; the two oxyhydroxides boehmite

( $\gamma$ -AlOOH), and diaspore ( $\alpha$ -AlOOH); and the most dehydrated species akdalaite, also known as tohdite (5Al<sub>2</sub>O<sub>3</sub>·H<sub>2</sub>O or 2Al<sub>5</sub>O<sub>7</sub>(OH)) [1–3]. Fig. 1 illustrates the most common conversion paths for aluminum hydroxides. All aluminum hydroxides lead to stable  $\alpha$ -Al<sub>2</sub>O<sub>3</sub>, but only diaspore is a direct precursor. Gibbsite and boehmite, which are used as raw materials to produce alumina and a wide variety of other industrial products, are the aluminum hydroxides of highest practical value. Nanostructured gibbsite and boehmite have a thermal stability that is consistent with the thermal stability of their bulk phases, at least for temperatures up to 350 °C, as was shown by Zhang et al. [8]. The use of boehmite nanosheets for improving membrane-based effluent treatment technologies, for which they hold great promise in terms of environmental sustainability, is an example of a most promising application of a nanoscale aluminum hydroxide: Zavabeti et al. obtained boehmite nanosheets through a green and scalable synthesis method, and demonstrated that these can be used to fabricate membrane filters that show an excellent separation of heavy metal ions and oils from aqueous solutions at extraordinary flux [9].

There have been many previous studies of aluminum oxides and aluminum hydroxides. Here just a few works will be named, with no intention of a complete review. A review of experimental studies of bulk phases can be found in the recent works by Busca [2], and Chandran

E-mail address: [h.vangog@tudelft.nl](mailto:h.vangog@tudelft.nl).

<https://doi.org/10.1016/j.apsusc.2020.148501>

Received 5 September 2020; Received in revised form 13 November 2020; Accepted 14 November 2020

Available online 21 November 2020

0169-4332/© 2020 The Author. Published by Elsevier B.V. This is an open access article under the CC BY license (<http://creativecommons.org/licenses/by/4.0/>).

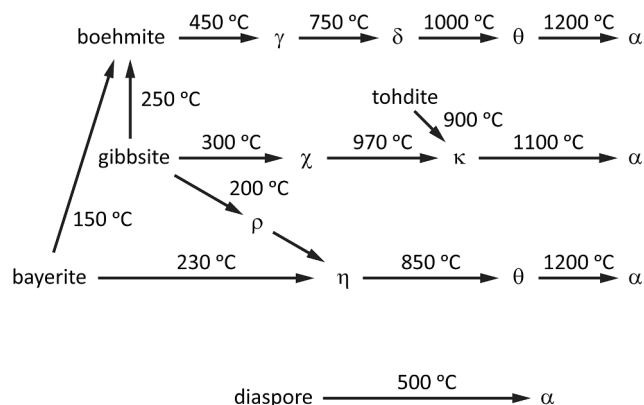


Fig. 1. The transformation sequences that are most common for aluminum oxides and hydroxides [1–3]. Greek letters indicate aluminas. Included are indicative values of the transition temperatures.

et al. [1]. Busca discusses the synthesis and properties of various nanostructured phases as well. A review of the methods reported in the literature for the synthesis of nanostructured  $\gamma$ - $\text{Al}_2\text{O}_3$  and nanostructured boehmite can also be found, for example, in works by Bell et al. [10,11], and in the already mentioned work by Zavabeti et al. [9]. Comprehensive computational studies using hybrid density functional theory (DFT) were carried out on aluminum hydroxides by Demicheli et al. [12], and on aluminum oxides and hydroxides by Peintinger et al. [13]. Nagendran et al. investigated  $\text{Al}(\text{OH})_3$  by means of DFT calculations including van der Waals corrections, and identified three new polymorphs of  $\text{Al}(\text{OH})_3$  besides the four known polymorphs, which provides an opportunity of targeted synthesis of new aluminum trihydroxides [14]. The dehydration process of aluminum hydroxides has been investigated computationally as well: Krokidis et al. studied the transformation mechanism of the dehydration of boehmite to  $\gamma$ - $\text{Al}_2\text{O}_3$  using DFT and *ab initio* molecular dynamics (AIMD) simulations, without observing the actual formation and release of  $\text{H}_2\text{O}$ , however [15].

The kinetics and transformation mechanisms of the thermal dehydration of aluminum hydroxides are a subject of ongoing research. A large measure of agreement has been reached on the transformation sequences. Less information is available on the kinetics of the dehydration processes, however, and little is known about the transformation mechanisms. Investigation of interfaces between dehydrated phases and their hydrated precursors could be helpful in elucidating reaction pathways. Partial dehydration results in the formation of interfaces. Most experimental studies of partially dehydrated aluminum hydroxides, however, are unable to observe actual interfaces in the investigated samples, and were found to report pseudomorphosis relationships only. Löffler et al. [16] are an exception in this regard (the only one found during the literature search for this study). These authors studied the dehydration of diaspore by means of transmission electron microscopy (TEM), and provided TEM images and a schematic representation of the reaction interface observed in partially dehydrated diaspore crystals. Computational studies of interfaces were not found at all. The present study, dedicated to the computational identification and characterization in terms of energetic stability and atomic configuration of possible interface geometries, is intended as a first step to filling this gap in the literature.

The present study was carried out using plane-wave DFT simulations. In general, *ab initio* methods are considered more accurate than simulation methods that depend on empirical potentials that have been parametrized. DFT methods also allow the monitoring of chemical bonding and bond-breaking processes that, for example, force-field molecular dynamics (MD) methods are incapable of simulating with sufficient predictive power. Force-field MD calculations are considered

more suitable, on the other hand, when simulating large numbers of atoms, as the increased accuracy and predictive power of quantum mechanical methods come at a computational cost that usually makes them too inefficient to handle large systems. MD methods are also capable of still finding the thermodynamically most stable configuration when DFT methods, for which starting configurations are required that are already close to reality before relaxation, no longer can.

The interface systems considered here, indeed contain quite a number of atoms. Nonetheless, test calculations performed prior to the study to assess the computational cost of DFT calculations, as the computational cost, due to the valence electron configurations for the H and Al atoms, present in large numbers in the interface systems, might still be reasonable, clearly pointed to computational feasibility of DFT simulation of these interface systems. The possibility of observing bond-breaking and bonding processes related to dehydration at the interfaces was highly valued; that DFT simulation might not result in the thermodynamically most stable configurations was therefore accepted. (On a side note, it was found that certain atoms actually did migrate over quite large distances during relaxation.) As a result of the choice for DFT simulations, this paper could be written in its present form, and report, for example, the formation of (chemisorbed)  $\text{H}_2\text{O}$  molecules and the observed route of their formation during relaxation, which would not have been possible if a force-field MD method had been used instead.

The subject of the present investigation are interfaces between diaspore and  $\alpha$ - $\text{Al}_2\text{O}_3$ , boehmite and  $\gamma$ - $\text{Al}_2\text{O}_3$ , and boehmite and gibbsite. The choice of these particular bulk phases is motivated by the fact that diaspore and boehmite are the direct precursors of  $\alpha$ - $\text{Al}_2\text{O}_3$  and  $\gamma$ - $\text{Al}_2\text{O}_3$ , which are the thermodynamically stable and most prominent transition alumina, respectively, while gibbsite is the most common aluminum hydroxide and transforms to boehmite. Using plane-wave DFT calculations and employing the optB88-vdW density functional [17,18] to account for van der Waals interactions, the atomic configuration of eight possible interface configurations was determined. Seven of these are linked to phase orientation relationships that were found reported in previous experimental works on the dehydration of diaspore, gibbsite, and boehmite under hydrothermal-atmospheric conditions or during heat-treatment in air [16,19,20]. One interface based on a previous study of the transformation of gibbsite into boehmite under hydrothermal conditions in an aqueous suspension was also investigated [21], for comparison. The stability of the interface configurations was studied by calculation and comparison of interface energies. A Bader charge analysis [22] was performed to study interface charge effects. The route of formation of dehydration-related interface defects during relaxation was observed and analyzed. The results will be discussed in the light of previous investigations of alumina hydrate dehydration.

The dehydration processes of the various aluminum hydrate phases are complex, multi-scale, and multi-stage processes. The present study does not claim to describe nucleation and growth, or even the time evolution of the dehydration processes. To investigate all these phenomena in a single simulation study would be an impossible task. Full understanding of the dehydration processes must come from multiple studies where various aspects of the processes are investigated from different viewpoints and necessarily employing different methods. The high-accuracy DFT results presented here contribute to the overall understanding of the energy landscape underlying the dehydration phenomena, and provide details (the formation of particular defects and of water molecules at the interface, and accumulation of charge density, for example) that would be lost when less accurate scaled-up methods would be used. Temperature-induced system fluctuations are beyond the scope of the present study. Numerous suggestions are included, however, for follow-up studies that do take dynamic and temperature effects into account and that can benefit from the insights obtained from the present work. Combined, this will eventually lead to multi-scale insights and insights into the time evolution of the dehydration processes, and hopefully one day to the full understanding of the dehydration mechanisms of aluminum hydrates.

## 2. Computational methodology

### 2.1. Bulk phase unit cells

Not all bulk phases that are considered in this study have been fully characterized yet. In this section the structural models and unit cells that were used for the aluminum oxides and hydroxides will be shortly discussed. Illustrations of the bulk phases can be found as Supporting Fig. S1 in the Supporting Information. The selection of potential interface geometries and the construction of corresponding interface simulation supercells will be described in Section 2.2.

The crystal structures of corundum and diaspore are well known. Corundum crystallizes in a trigonal structure with space group  $R\bar{3}c$  and can be described using either a rhombohedral or a hexagonal lattice system [23]. Here, the hexagonal description is used, in which one unit cell contains 30 atoms (see Fig. S1a). The unit cell of diaspore is an orthorhombic one with space group  $Pbnm$  [24] and contains four  $AlO(OH)$  units (see Fig. S1b). The precise location of the hydrogen atoms in boehmite, and therefore the space group of boehmite, is not fully known. Here, a unit cell in  $Cmc2_1$  symmetry and containing 16 atoms was used (see Fig. S1c): of the various structures considered in the literature for boehmite, space group  $Cmc2_1$  yields the most symmetric lowest-energy configuration and was found to better describe the boehmite structure than the more frequently quoted space group  $Cmcm$  [12]. Although not with high accuracy, the positions of the hydrogen atoms in gibbsite are known; the unit cell of gibbsite contains eight  $Al(OH)_3$  units (see Fig. S1d) and possesses  $P2_1/n$  symmetry [25].

The precise structure of  $\gamma-Al_2O_3$  is still under scientific debate [1,2,13]. Traditionally,  $\gamma-Al_2O_3$  is described as a defective cubic spinel structure displaying  $Fd\bar{3}m$  symmetry, in which the oxygen atoms form a cubic close-packed sublattice and the aluminum atoms are located at tetrahedral and octahedral interstitial sites. To produce the correct stoichiometry of  $\gamma-Al_2O_3$ , cation vacancies are needed, i.e., the spinel has to be defective. The tetrahedral-octahedral ratio of cation vacancies, however, heavily depends on synthesis conditions; and aluminum cations have been reported to occupy 'nonspinel' positions as well (see the discussion in Busca [2], Peintinger et al. [13], and Chandran et al. [1], and references cited therein). Most  $\gamma-Al_2O_3$  samples are also found to show a tetragonal distortion, and a recent experimental study suggests that this tetragonal distortion could be an intrinsic property of  $\gamma-Al_2O_3$  regardless of synthesis method [26]. At present, the spinel models by Paglia et al. [27] are in general considered to be the best structural models available [13,28–30]. These models each contain 160 atoms in their unit cell, and possess  $Fd\bar{3}m$  and  $I4_1/amd$  symmetry. Boehmite-derived  $\gamma-Al_2O_3$ , which is the  $\gamma-Al_2O_3$  of interest here, was found to be best described by the latter [31,32]. For the present DFT calculations of large interface systems, however, a  $\gamma-Al_2O_3$  bulk phase simulation unit cell with less than 160 atoms was to be preferred. Here, the model proposed by Krokidis et al. [15] and published by Digne et al. [33] has been used. This nonspinel model was found to be more stable than traditional spinel-type models. It consists of an orthorhombically distorted cubic close-packed oxygen sublattice and aluminum atoms that are located at nonspinel sites with a tetrahedral-octahedral coordination ratio of 1:3 and no structural vacancies (see Fig. S1e), and possesses  $P2_1/m$  symmetry. With a unit cell of 40 atoms, for the present study, this model is a good compromise between structural reliability and computational costs.

### 2.2. Interface supercells

The interfaces that were simulated in this study are all linked to phase orientation relationships that have been reported in previous experimental studies. In general, within any one phase orientation relationship, numerous interfaces with various interface orientations are possible. As this investigation is intended as a first exploration, the

present study has been limited to the interfaces that are the most straightforward within a given phase orientation relationship. In total three diaspore/corundum interfaces (supercells 1–3), one boehmite/ $\gamma-Al_2O_3$  interface (supercell 4), and four gibbsite/boehmite interface configurations (supercells 5–8) were investigated.

Table 1 provides an overview of the interface simulation supercells that were used in this study. The construction of the supercells will be discussed into more detail below after the more general comments on their construction in this paragraph. The simulated configurations are all interface configurations that, based on considerations of lattice mismatch, common symmetry, atomic coherence, and number of defects at the interface, have a reasonable probability of occurring. During the construction of the interface supercells extra care was taken to ensure atomic coherence with regard to the oxygen sublattice, as the symmetry of the oxygen network of the hydrated precursor governs the type of product formed after dehydration. Calculated resulting in-plane lattice mismatches are included in Table 1. Each interface input configuration was built as defect-free as possible from an integer number of bulk phase unit cells. The normal of the interface plane is always along the  $c$ -axis of the interface supercell. A minimum height of 15 Å along this axis was ensured for each bulk phase component. Within one supercell, bulk component slabs are about the same height. The consequent number of unit cells and the total number of atoms in a supercell required for the construction of the supercell in accordance with the criteria mentioned above, can be found in Table 1 as well.

Only for the diaspore/corundum interface a previous experimental study describing the dehydration interface geometry could be found. This study is the earlier mentioned study by Löffler et al. [16], who investigated the dehydration of diaspore during heat-treatment in air. The geometry reported by these authors, however, is a reaction interface geometry, with cracks and pore lamellae and features at the micrometer scale, and as such unsuitable for modelling and simulation in the present study. For the construction of the diaspore/corundum interface supercells, the reported orientation relationship was therefore used as a starting point instead. The orientation relationship for diaspore and corundum is well known: during dehydration, the  $a$ ,  $b$  and  $c$  axes of diaspore transform into the  $c$ ,  $[11\bar{2}0]$  and  $[\bar{1}100]$  axes of corundum, respectively. The most straightforward interfaces within this orientation relationship are a diaspore(100)//corundum(0001)  $\cap$   $[010]_D//[11\bar{2}0]_C$ , a diaspore(001)//corundum(1 $\bar{1}00$ )  $\cap$   $[010]_D//[11\bar{2}0]_C$ , and a diaspore(010)//corundum(1 $\bar{1}20$ )  $\cap$   $[001]_D//[\bar{1}100]_C$  interface. The supercells simulating these three interfaces are illustrated in Fig. S2a–c. As can be seen, in supercell 1, the diaspore (100) and the corundum (0001) planes are parallel to the plane of the interface; whereas in supercells 2 and 3, these planes are perpendicular to the plane of the interface, and the bases of the hexagons that form the hexagonal oxygen sublattices are parallel and perpendicular, respectively, to that plane.

Three of the four possible gibbsite/boehmite interface configurations considered in this study are simulated by supercells 5–7. These simulation cells are all based on the preferred crystal orientations reported by Saalfeld [19], who studied the dehydration of gibbsite to boehmite in a hydrothermal atmosphere. Supercell 5 is illustrated in Fig. S2e. This supercell simulates an interface geometry that results from the continuation of the pseudohexagonal oxygen sublattice of gibbsite across the interface into the boehmite structure. Whereas all other supercells used in this study consist of an integer number of bulk phase unit cells and contain integer numbers of formula units, the interface in supercell 5 could not be constructed in an atomically coherent way without adding 4 Al atoms (see Table 1). Supercells 6 and 7 simulate interfaces in which the gibbsite and boehmite octahedral layers are octahedrally linked across the interface. The double sheets of  $AlO_6$  octahedra of the boehmite structure are perpendicular to the interface plane in supercell 6 (Fig. S2f), and parallel to that plane in supercell 7 (Fig. S2g). As can be seen from Fig. S2f, the interface simulated by supercell 6 is an interface that is dislocation-free, whereas the interface simulated by supercell 7

**Table 1**

Input configuration details of the interface simulation supercells. The interface plane direction is along the  $c$ -axis of the supercell. In-plane lattice mismatches  $\delta_a$  and  $\delta_b$  are the lattice mismatch along the  $a$ - and  $b$ -axis direction of the supercell calculated from the optB88-vdW-obtained bulk phase unit cell lattice parameters.  $N_D$ ,  $N_C$ ,  $N_\gamma$ ,  $N_B$ , and  $N_G$ , denote one unit cell of diaspore, corundum,  $\gamma$ - $\text{Al}_2\text{O}_3$ , boehmite, and gibbsite, respectively.

Supercell	$c$ -axis	$a$ -axis	$\delta_a$ (%)	$b$ -axis	$\delta_b$ (%)	Unit cells N in supercell	Atoms
Supercell 1	$[100]_D // [0001]_C$	$[010]_D // [11\bar{2}0]_C$	1.3	$[001]_D // [\bar{1}100]_C$	3.4	$18 N_D + 4 N_C$	528
Supercell 2	$[001]_D // [1\bar{1}00]_C$	$[010]_D // [11\bar{2}0]_C$	1.3	$[\bar{1}00]_D // [0001]_C$	1.2	$18 N_D + 4 N_C$	528
Supercell 3	$[010]_D // [11\bar{2}0]_C$	$[001]_D // [\bar{1}100]_C$	3.4	$[100]_D // [0001]_C$	1.2	$18 N_D + 4 N_C$	528
Supercell 4	$[201]_\gamma // [025]_B$	$[010]_\gamma // [100]_B$	3.4	$[\bar{1}01]_\gamma // [01\bar{4}]_B$	2.2	$12 N_\gamma + 39 N_B$	1104
Supercell 5	$[001]_G // [025]_B$	$[010]_G // [0\bar{1}4]_B$	5.7	$[\bar{1}00]_G // [100]_B$	0.1	$12 N_G + 39 N_B + 4 \text{ Al}$	1300
Supercell 6	$[0\bar{7}3]_G // [001]_B$	$[100]_G // [100]_B$	0.1	$[032]_G // [010]_B$	1.7	$23 N_G + 72 N_B$	2440
Supercell 7	$[0\bar{7}3]_G // [010]_B$	$[100]_G // [100]_B$	0.1	$[032]_G // [00\bar{1}]_B$	9.1	$23 N_G + 72 N_B$	2440
Supercell 8	$[001]_G // [010]_B$	$[100]_G // [100]_B$	0.1	$[010]_G // [00\bar{1}]_B$	2.0	$6 N_G + 24 N_B$	720

(see Fig. S2g) contains dislocations and has a large in-plane lattice mismatch (see Table 1). A simulation cell for the latter without dislocations and/or a smaller in-plane lattice mismatch could not be established, however, without exceeding the limit of computational feasibility of this study. Supercells 6 and 7 are the largest simulation cells used in the present investigation.

The fourth gibbsite/boehmite interface is not based on an orientation relationship reported for the dehydration of gibbsite during heat-treatment in air or under hydrothermal-atmospheric conditions, but is linked to a study of Egorova et al. [21], who investigated the dissolution and recrystallization of gibbsite into boehmite during hydrothermal treatment in an aqueous suspension. The mechanism suggested by these

authors for the observed transition consists of delamination and subsequent dissolution of (001) gibbsite planes, and the successive precipitation of boehmite crystals along the (001) plane of gibbsite crystals. The gibbsite(001)//boehmite(010) interface of supercell 8 is based on this suggested mechanism. In this interface configuration, the single  $\text{AlO}_6$  octahedra sheets of gibbsite and the double  $\text{AlO}_6$  octahedra sheets of boehmite are both parallel to the plane of the interface (Fig. S2h). Because of the dissolution-precipitation mechanism, the criterion of atomic coherence across the interface was not applied here.

In addition to the interfaces described above, one possible boehmite/ $\gamma$ - $\text{Al}_2\text{O}_3$  dehydration interface configuration was investigated, using supercell 4. As can be seen from Fig. S2d, this supercell was, similarly to

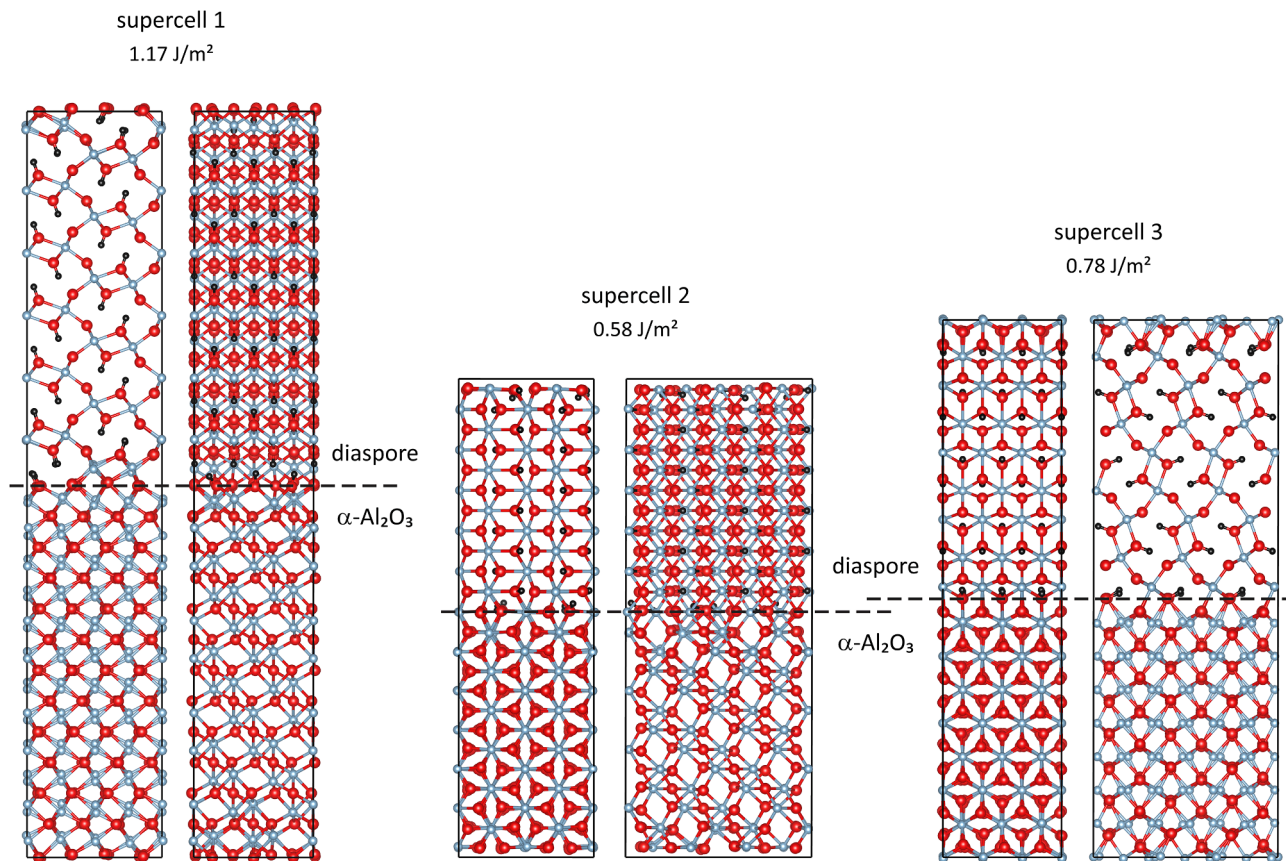


**Fig. 2.** The supercells simulating the diaspore/corundum interfaces as obtained after full relaxation. For each supercell, the [010] (left) and [100] (right) projection are shown. Light blue, red, and black spheres denote Al, O, and H atoms, respectively. The boundaries of the simulation cells are indicated with black solid lines. Dashed lines indicate the interfaces at  $Z_{\text{rel}} \approx 1/2$ . Included are the values of the calculated interface energy. (For interpretation of the references to colour in this figure legend, the reader is referred to the web version of this article.)

the hexagonally aligned gibbsite/boehmite interface configuration of supercell 5, obtained by matching the pseudo-hexagonal oxygen sublattices present in boehmite and  $\gamma$ -Al<sub>2</sub>O<sub>3</sub>. The orientation of this interface can be linked to the phase orientation relationship reported for the dehydration of boehmite to  $\gamma$ -Al<sub>2</sub>O<sub>3</sub> during heat-treatment in air in a previous study by Wilson [20].

### 2.3. Computational details

The DFT calculations were carried out using the first-principles Vienna Ab initio Simulation Package (VASP) [34–36]. The performance of four functionals and methods was investigated. Within the projector augmented wave framework (PAW) [37,38], the generalized gradient approximation (GGA) functional [39] by Perdew, Burke, and Ernzerhof (PBE) was employed to allow for a semilocal treatment of the exchange and correlation. As GGA-PBE does not take into account van der Waals interactions and results in lower accuracy for hydrogen-bonded layered systems [40], the optB88-vdW density functional by Klimeš et al. [18] (optB88-vdW) was also employed. The optB88-vdW density functional, being the van der Waals density functional by Dion et al. [17] (vdW-DF) optimized by using an optimized Becke88

$$E_{\text{int}} = \frac{E_{\text{super}}[\text{Al}_{m+k+q}\text{O}_{2m+3k}\text{H}_{3k}] - m \cdot E_{\text{unit}}[\text{AlOOH}] - k \cdot E_{\text{unit}}[\text{Al}(\text{OH})_3] - q \cdot E_{\text{unit}}[\text{Al}]}{2 \cdot A_{\text{int}}} \quad (2)$$

approximation for the GGA exchange component, accounts for nonlocal electron correlation effects due to London dispersion interactions, and has been applied successfully to various systems [41–45]. The DFT-D3 correction method of Grimme [46] includes dispersive interactions by adding a parametrized dispersion correction energy term to the self-consistently calculated electronic energy and was applied here as well, in combination with the PBE functional and with zero damping. The performance of the more advanced Hartree-Fock/DFT hybrid Heyd-Scuseria-Ernzerhof HSE06 functional [47] was also investigated. The calculations of the aluminum oxide and aluminum hydroxide reference bulk phases were carried out with application of the functionals and methods mentioned above. On the supercells, only optB88-vdW calculations were performed.

The calculations were conducted at a level of accuracy sufficient for studying structural properties and total energies. Different  $k$ -meshes and cutoff energies were tested to ensure energy convergence well within 1 meV/atom for the bulk phase unit cells. For the PBE, optB88-vdW, and DFT-D3 calculations, the cutoff energy of the wave functions was set to 750 eV and a cutoff energy of 1050 eV was used for the augmentation functions. The Brillouin zone was sampled, and  $\Gamma$ -centered in the case of the hexagonal unit cell of corundum, using the Monkhorst and Pack scheme [48] and ensuring a linear  $k$ -point spacing of less than 0.05 Å<sup>-1</sup> for each  $k$ -mesh. Table S1 lists the  $k$ -mesh sizes that were used for the simulations. For the HSE06 calculations, the cutoff energy of the wave functions and the augmentation functions were set to 500 and 700 eV, respectively, and  $k$ -meshes with a linear  $k$ -point spacing of less than 0.09 Å<sup>-1</sup> were used. The fraction of Hartree-Fock exchange for these calculations was set to 0.30. For all calculations, potentials with 3s<sup>2</sup>3p<sup>1</sup>, 2s<sup>2</sup>2p<sup>4</sup>, and 1s<sup>1</sup> valence electron configuration were adopted for the Al, O, and H atoms, respectively.

All structures were structurally optimized to yield lower-energy configurations. For the bulk phase unit cell simulations, an energy convergence criterion of 10<sup>-5</sup> eV was applied for the ionic relaxation loop and an energy convergence criterion of 10<sup>-6</sup> eV for the electronic convergence loop. For the supercell simulations, criteria of 10<sup>-4</sup> and 10<sup>-5</sup> eV were used. Resulting atomic forces for the supercells can be

found in Table S1. To study interface charge effects, a Bader charge analysis was carried out. Bader [22] defines the boundary of an atom as the surface where the normal component of the gradient of the electron density is zero. The charge within the volume enclosed by this surface is interpreted as the electronic charge of the atom. The Bader charge analysis was performed using the approach by Henkelman et al. [49–51]. All calculations are valid for a temperature of 0 K and a pressure of 0 Pa. Zero-point vibration contributions have been neglected.

### 2.4. Definition of formation energy

Because of the periodic boundary conditions that apply to plane-wave DFT calculations, each interface supercell contains two interfaces: one at  $Z_{\text{rel}} \approx 0$  and another at  $Z_{\text{rel}} \approx 1/2$ . The interface energy  $E_{\text{int}}$  of the simulated diaspore/corundum and boehmite/ $\gamma$ -Al<sub>2</sub>O<sub>3</sub> interfaces, evaluated with respect to the appropriate oxide and hydroxide reference bulk phases, can therefore be calculated as:

$$E_{\text{int}} = \frac{E_{\text{super}}[\text{Al}_{2n+m}\text{O}_{3n+2m}\text{H}_m] - n \cdot E_{\text{unit}}[\text{Al}_2\text{O}_3] - m \cdot E_{\text{unit}}[\text{AlOOH}]}{2 \cdot A_{\text{int}}}, \quad (1)$$

and the interface energy of the gibbsite/boehmite interfaces as:

Here,  $E_{\text{super}}$  is the total energy of the supercell;  $E_{\text{unit}}[\text{Al}_2\text{O}_3]$ ,  $E_{\text{unit}}[\text{AlOOH}]$ , and  $E_{\text{unit}}[\text{Al}(\text{OH})_3]$  are the energies of one unit of Al<sub>2</sub>O<sub>3</sub>, AlOOH, and Al(OH)<sub>3</sub>;  $E_{\text{unit}}[\text{Al}]$  is the energy of one bulk phase Al atom;  $n$ ,  $m$ , and  $k$  are the number of Al<sub>2</sub>O<sub>3</sub>, AlOOH, and Al(OH)<sub>3</sub> units in the supercell;  $q$  is the number of additional Al atoms added to the supercell (*i.e.*,  $q$  is 4 for supercell 5, and 0 for all other supercells); and  $A_{\text{int}}$  is the area of the interface calculated from the supercell lattice vectors  $a$  and  $b$  as  $A_{\text{int}} = |a \times b|$ . Note that for supercells in which the two interfaces are not equivalent, the calculated interface energy is the averaged value of the interface energy of these two interfaces.

## 3. Results and discussion

### 3.1. Description of the bulk phases

Table 2 provides a summary of the PBE-, optB88-vdW-, DFT-D3-, and HSE06-calculated structure parameters for the bulk phase unit cells used in this study. Experimentally determined values can be found in Table 2 as well. As can be seen, the PBE calculations resulted in an overestimation of the bulk phase lattice parameters, which is a known feature of GGA functionals. The optB88-vdW, DFT-D3, and HSE06 approaches, which include nonlocal effects to a larger extent than GGA approaches do, successively led to smaller values, and resulted in an underestimation of the lattice parameters of gibbsite by DFT-D3, and of all considered phases by HSE06. The predicted values of the lattice parameters of boehmite and gibbsite that are along the stacking direction of the hydrogen-bonded layers in these structures, show a different trend: For the  $b$  parameter of boehmite and the  $c$  parameter of gibbsite, PBE calculation resulted in values that are already smaller than the experimentally determined values. This underestimation increased when using the optB88-vdW and DFT-D3 approaches. Application of the HSE06 functional produced better estimates than the latter two, but was found to produce worse estimates than PBE calculation.

The results are in good agreement with previous simulation results

**Table 2**

Bulk phase unit cell parameters and electronic band gap. Listed are the values calculated in this study using four different functionals/methods. Corundum is given in hexagonal description. Results from previous experimental and computational studies are included for comparison.

Bulk phase (Space group)	Property	This Work GGA-PBE	This Work optB88-vdW	This Work DFT-D3	This Work HSE06	Previous Exp.	Previous vdW-DF	Previous DFT-D
Corundum ( $R\bar{3}c$ )	$a$ (Å)	4.805	4.801	4.784	4.745	4.761 <sup>a</sup>	4.840 <sup>b</sup>	4.806 <sup>j</sup>
	$c$ (Å)	13.114	13.095	13.057	12.956	12.996 <sup>a</sup>	13.211 <sup>b</sup>	13.162 <sup>i</sup>
	$V$ (Å <sup>3</sup> )	262.25	261.38	258.82	252.64	255.05 <sup>a</sup>	268.06 <sup>b</sup>	263.28 <sup>i</sup>
	$E_g$ (eV)	5.9	6.4	6.0	8.6	8.5–8.8 <sup>b</sup>	—	—
Diaspore ( $Pbnm$ )	$a$ (Å)	4.430	4.416	4.392	4.392	4.401 <sup>c</sup>	—	—
	$b$ (Å)	9.502	9.479	9.454	9.381	9.425 <sup>c</sup>	—	—
	$c$ (Å)	2.872	2.869	2.854	2.833	2.845 <sup>c</sup>	—	—
	$V$ (Å <sup>3</sup> )	120.87	120.09	118.51	116.71	118.01 <sup>c</sup>	—	—
	$E_g$ (eV)	6.0	6.4	6.2	9.4	—	—	—
$\gamma$ -Al <sub>2</sub> O <sub>3</sub> ( $P2_1/m$ )	$a$ (Å)	5.579	5.566	5.546	5.510	—	—	5.568 <sup>j</sup>
	$b$ (Å)	8.401	8.381	8.357	8.292	—	—	8.393 <sup>i</sup>
	$c$ (Å)	8.072	8.066	8.033	7.975	—	—	8.055 <sup>i</sup>
	$\beta$ (°)	90.52	90.64	90.59	90.51	—	—	90.63 <sup>i</sup>
	$V$ (Å <sup>3</sup> )	378.30	376.24	372.32	364.37	—	—	376.41 <sup>i</sup>
	$E_g$ (eV)	4.9	5.4	5.0	8.2	7.6–8.7 <sup>d</sup>	—	—
Boehmite ( $Cmc2_1$ )	$a$ (Å)	2.895	2.891	2.876	2.858	2.876 <sup>e</sup>	2.916 <sup>b</sup>	—
	$b$ (Å)	12.140	12.049	11.944	12.085	12.24 <sup>e</sup>	12.424 <sup>b</sup>	—
	$c$ (Å)	3.735	3.728	3.726	3.691	3.709 <sup>e</sup>	3.749 <sup>b</sup>	—
	$V$ (Å <sup>3</sup> )	131.27	129.87	127.99	127.45	130.57 <sup>e</sup>	135.83 <sup>b</sup>	—
	$E_g$ (eV)	5.6	5.9	5.8	8.7	7.5–8.8 <sup>f</sup>	—	—
	$E_g$ (eV)	5.2	5.5	5.4	8.1	7.3–8.5 <sup>f</sup>	—	—
Gibbsite ( $P2_1/n$ )	$a$ (Å)	8.766	8.685	8.665	8.643	8.684 <sup>g</sup>	8.814 <sup>b</sup>	—
	$b$ (Å)	5.108	5.075	5.056	5.049	5.078 <sup>g</sup>	5.154 <sup>b</sup>	—
	$c$ (Å)	9.690	9.603	9.558	9.646	9.736 <sup>g</sup>	9.864 <sup>b</sup>	—
	$\beta$ (°)	92.64	93.33	92.69	92.61	94.54 <sup>g</sup>	93.49 <sup>b</sup>	—
	$V$ (Å <sup>3</sup> )	433.45	422.51	418.29	420.50	427.98 <sup>g</sup>	447.30 <sup>b</sup>	—
	$E_g$ (eV)	5.2	5.5	5.4	8.1	7.3–8.5 <sup>f</sup>	—	—

<sup>a</sup> Ref. [76].

<sup>b</sup> Refs. [54,55].

<sup>c</sup> Ref. [24].

<sup>d</sup> Refs. [56,57].

<sup>e</sup> Ref. [77].

<sup>f</sup> Ref. [58].

<sup>g</sup> Ref. [25].

<sup>h</sup> Ref. [28]. Boehmite was described in  $Cmcm$  symmetry and with antiparallel O—H...O chains. The study reports cell volumes only. Lattice parameters were kindly provided upon request.

<sup>i</sup> Ref. [53].

reported in the literature, as can be seen from the comparison with, for example: Demichelis et al., who assessed the performance of 12 LDA, GGA, and hybrid functionals in describing diaspore, boehmite, and gibbsite [40]; Platonenko et al., who investigated the accuracy of 6 different pure and hybrid DFT functionals for corundum [52]; Ferreira et al., who studied the effects of two GGA functionals and the original vdW-DF van der Waals density functional by Dion et al. on the description of corundum, boehmite, and gibbsite [28]; and Conesa, who compared the results from standard PBE and DFT-D dispersion-corrected PBE calculations for corundum and  $\gamma$ -Al<sub>2</sub>O<sub>3</sub> [53]. The vdW-DF- and DFT-D-obtained values from the latter two studies are included in Table 2. The results by Ferreira et al. appear to be in contrast to the findings here. Those authors found the van der Waals density functional they applied to result in larger values for lattice parameters and cell volume than the PBE functional, whereas in the present study the employed van der Waals density functional was found to produce smaller values than the PBE functional. This difference may be caused, however, by the specific functionals used: while Ferreira et al. used the original functional by Dion et al., here an optimized version of that functional was used.

The simulation studies mentioned in the previous paragraph all compared the performance of GGA with either hybrid, vdW-DF, or DFT-D methods. The present study, however, allows for a direct comparison between the latter three types of methods as well. The previous study by Demichelis et al. showed that the presence of H atoms and the layered nature of a structure may introduce substantial differences in the behavior of functionals [40]. The findings from the present study are a

clear illustration of this. Comparing the PBE, optB88-vdW, DFT-D3, and HSE06 results, we find that, in terms of lattice parameters and unit cell volume: corundum, without H atoms and not a layered structure, is best described by HSE06, then DFT-D3, then optB88-vdW, then PBE; diaspore, with H atoms but not a layered structure, is best described by DFT-D3, then HSE06, then optB88-vdW, then PBE; boehmite, with H atoms and a layered structure without intralayer hydrogen bonds, is overall best described by PBE and optB88-vdW, then DFT-D3, then HSE06; and gibbsite, with H atoms and a layered structure with interlayer and intralayer hydrogen bonds, is overall best described by PBE and optB88-vdW, then HSE06, then DFT-D3.

The electronic band gaps were also calculated. As can be seen from Table 2, unlike the structural parameters results, the band gap results show a clear trend for the functionals and methods applied in this study. The PBE functional was found to result in a significant underestimation of the band gap, which is a notorious trait of DFT methods. The optB88-vdW functional and the DFT-D3 method were found to be an improvement compared to PBE, with optB88-vdW outperforming DFT-D3, but still resulted in considerable underestimations. The HSE06-calculated values, on the other hand, are in good agreement with experimental values [54–58], and compare well with previous simulation results from hybrid functionals [13,52,58].

Including dispersion interactions in the DFT calculations of the aluminum oxide and aluminum hydroxide bulk phases resulted in an overall better prediction of the structure parameters and band gaps of these structures. Therefore, for the present study of aluminum oxide and

**Table 3**

Net atomic Bader charges ( $e$ ) in the bulk phase structures. Al<sub>oct</sub>: octahedrally coordinated Al atom. Al<sub>tet</sub>: tetrahedrally coordinated Al atom. O<sub>Al</sub>: O atom coordinated by Al atoms only. O<sub>Al+hb</sub>: O atom coordinated by 3 Al atoms and with a fourth coordination site involved in hydrogen-bonding. O<sub>Al+H</sub>: O atom coordinated by 3 Al atoms and 1H atom. O<sub>Al+H+hb</sub>: O atom coordinated by 2 Al atoms and 1H atom and with a fourth coordination site involved in hydrogen-bonding.

Atom	Corundum	$\gamma$ -Al <sub>2</sub> O <sub>3</sub>	Diaspore	Boehmite	Gibbsite
Al <sub>oct</sub>	+2.50	+(2.46–2.50)	+2.49	+2.49	+2.51
Al <sub>tet</sub>	–	+2.47	–	–	–
O <sub>Al</sub>	–1.67	–1.66	–	–1.66	–
O <sub>Al+hb</sub>	–	–	–1.61	–	–
O <sub>Al+H</sub>	–	–	–1.51	–	–
O <sub>Al+H+hb</sub>	–	–	–	–1.45	–(1.40–1.48)
H	–	–	+0.63	+0.62	+(0.58–0.63)

hydroxide interfaces, an approach that accounts for the nonlocal effects of dispersion was adopted. Out of the functionals and methods considered here, the optB88-vdW functional appeared to be the overall best choice. The interface supercells were calculated with this functional, and the remainder of this paper will report and refer to optB88-vdW-obtained values only.

### 3.2. Bader charge analysis of the bulk phases

To investigate the charge distribution among the atoms, electronic charge was assigned to the atoms according to the Bader partitioning scheme. The results of the Bader charge analysis of the bulk phases can be found in Table 3. As can be seen, in all bulk phase structures considered in this study, the Al atoms were found to have a net atomic Bader charge of  $\sim +2.5e$ . Tetrahedrally coordinated Al atoms are on average slightly less charged than octahedrally coordinated Al atoms, as was also found by previous simulation studies [12,28]. A Bader charge of  $\sim -1.65e$  was calculated for O atoms that are coordinated by Al atoms only. O atoms bonding to H atoms showed a decrease that can be understood as a cumulative reduction of this charge by  $\sim 0.05e$  when hydrogen-bonding to a H atom (*i.e.*, when forming an O $\cdots$ H bond) and by  $\sim 0.15e$  when covalently bonding to a H atom (*i.e.*, when forming the O–H bond in a hydroxyl group). On average, this is also true for gibbsite, although there, the O atoms of interlayer OH groups, which are oriented along the Z direction and whose O atoms are acceptors of intralayer hydrogen bonds, were found to be slightly more charged, at  $-(1.44\text{--}1.48)e$ , than the O atoms of intralayer OH groups, which lie approximately in the XY plane and whose O atoms are acceptors of interlayer hydrogen bonds, for which Bader charges of  $-(1.40\text{--}1.43)e$  were calculated. A decrease in charge due to the presence of an O–H bond has been observed experimentally in diaspore in a previous study by Hill, who found the protonated O atom in diaspore to have a considerably smaller net atomic charge than the non-protonated O atom [24]. The findings from the present study are in qualitative agreement with that study. The H atoms, finally, were found to have a Bader charge of  $\sim +0.6e$  (where in gibbsite, H atoms that are part of interlayer OH groups were found to be slightly more charged, at  $+(0.61\text{--}0.63)e$ , than H atoms that are part of intralayer OH groups and for which Bader charges of  $+(0.58\text{--}0.60)e$  were found). These values compare well with previous investigations as well [12,24].

### 3.3. Energetic stability of the interfaces

The calculated interface energies and the dimensions of the interface simulation cells as obtained after full relaxation, can be found in Table 4. As pointed out in the Introduction, the present DFT study may not have found the thermodynamically most stable configurations. The interface energies calculated for the obtained output configurations nonetheless appear to be very reasonable. Previously reported ceramic-ceramic interface energies could not be found in the literature. For metal-ceramic [59], metal-metal [60–62], and semiconductor-insulator [63] systems, however, previous studies have reported values ranging from 0.04 to 4.60 J/m<sup>2</sup>. The values obtained here are within that range. The

**Table 4**

Cell dimensions of the relaxed interface simulation supercells and calculated interface energy.

Supercell	$a$ (Å)	$b$ (Å)	$c$ (Å)	$E_{\text{int}}$ (eV/Å <sup>2</sup> )	$E_{\text{int}}$ (J/m <sup>2</sup> )
Supercell 1	9.555	8.463	52.824	0.073	1.17
Supercell 2	9.564	13.166	33.848	0.036	0.58
Supercell 3	8.453	13.137	38.273	0.048	0.78
Supercell 4	8.561	19.458	57.974	0.136	2.18
Supercell 5	19.610	8.750	60.076	0.108	1.72
Supercell 6	8.678	24.365	90.966	0.087	1.39
Supercell 7	8.689	22.616	96.869	0.142	2.27
Supercell 8	8.695	14.972	43.770	0.022	0.36

present interface configurations, with calculated interface energies of 0.36–2.27 J/m<sup>2</sup>, may therefore all be considered to have a reasonable probability of occurring.

The obtained output configurations are shown in Figs. 2–5. As can be seen, the diaspore/corundum interfaces were found to remain clean and sharp interfaces upon relaxation, their simulation cells showing only a very mild restructuring of atomic positions and cell dimensions. The supercells simulating the boehmite/ $\gamma$ -Al<sub>2</sub>O<sub>3</sub> and gibbsite/boehmite interfaces were found to show a much stronger restructuring. In some cases, the appearance of interface dehydration defects such as interstitial H and chemisorbed H<sub>2</sub>O was even observed. The interface energies calculated for these interfaces, *i.e.*, the values obtained from supercells 4, 5, and 7, are the interface energies of interfaces containing dehydration-related defects. A correction of these values to obtain interface energies of dehydration defect-free interfaces is not possible. It is estimated, however, that the effect of the dehydration defects on the calculated interface energies will be limited, considering the relatively large interface areas of the supercells simulating these interfaces.

The interface energy, calculated here as the energy required to form an interface from two bulk materials, consists of a chemical bonding and a structural strain part [59,64]. The chemical bonding part is the energy penalty for changing the chemical environment of the bulk materials at the interface. The structural strain component originates from the lattice mismatch between the two materials and the presence of misfit dislocations. These separate contributions to the interface energy cannot be calculated as individual components here. From Tables 1 and 4, however, the effect of the in-plane lattice mismatch on the interface energy can be unmistakably observed. The in-plane lattice mismatches and the calculated interface energies of the diaspore/corundum interfaces (supercells 1–3), for example, clearly show how the interface energy increases with increasing lattice mismatch. The same effect can be seen from the comparison of the gibbsite/boehmite interfaces of supercells 6 and 7, although it should be noted that the larger in-plane lattice mismatch of the latter is interconnected with the presence of misfit dislocations at the interface.

The chemical bonding component is nicely illustrated by the results from supercells 6 and 8. These two supercells simulate gibbsite/boehmite interfaces with nearly identical in-plane lattice mismatches, and neither was found to contain dehydration-related defects upon relaxation. Their calculated interface energies differ greatly, however.

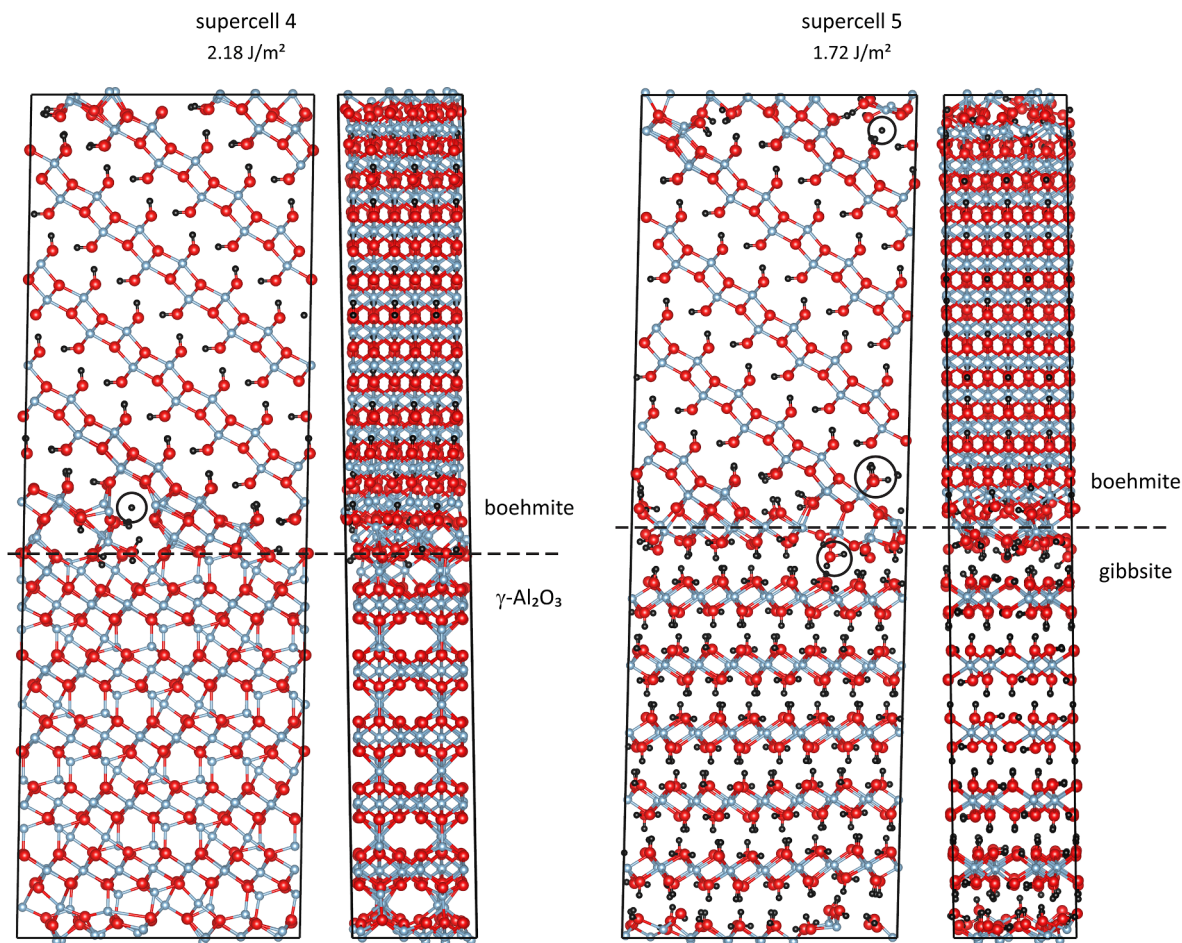


**Fig. 3.** The output configurations of supercells 4 and 5. For supercell 4, the  $[1\bar{1}00]$  (left) and  $[0\bar{1}0]$  (right) projections are shown. For supercell 5, the  $[010]$  (left) and  $[100]$  (right) projections are shown. The boundaries of the simulation cells are indicated with black solid lines. Dashed lines indicate the interfaces at  $Z_{\text{rel}} \approx 1/2$ . Light blue, red, and black spheres denote Al, O, and H atoms, respectively. Circled in black are, in supercell 4: one H interstitial; and in supercell 5: one H interstitial, one OH<sub>2</sub> group, and one chemisorbed H<sub>2</sub>O molecule. Included are the values of the calculated interface energy. (For interpretation of the references to colour in this figure legend, the reader is referred to the web version of this article.)

This must for a large part be caused by their difference in interfacial chemical environment: the chemical environment of an interface resulting from the linkage of two atomically semicoherent oxygen sublattices (as in supercell 6) is obviously very different from the chemical environment of an interface that is the result of the hydrogen-bonding of two hydrogen-bonded layered bulk materials (as in supercell 8). The same effect must be present for supercells 1 and 3, albeit to a lesser degree as the difference in chemical environment of two interfaces that are both the result of the linkage of two atomically semicoherent sublattices, will be less pronounced.

As can be seen from [Tables 1 and 4](#), even the interfaces with a relatively large in-plane lattice mismatch were found to have a fairly low calculated interface energy (see, in particular, supercells 5 and 7). Experimental values, however, will likely be lower, as strain at the interface will be relieved by misfit dislocations.

From the point of view of dehydration, interfaces with a lower interface energy are not necessarily (more) involved in the dehydration process than interfaces with a higher interface energy. A lower interface energy indicates that an interface is thermodynamically more stable. Interfaces with a higher interface energy, on the other hand, will be more reactive, and may more easily form cracks and accommodate the release of water. It is interesting to compare the present simulation results in that regard with the experimental results of [Löffler & Mader \[16\]](#), who observed the transformation process of diasporite into corundum to occur much faster along the diasporite  $[010]$  direction than

it was found to take place along the other crystallographic directions. From the calculations, the diasporite(010)//corundum(11 $\bar{2}$ 0) interface of supercell 3 was indeed found to have an interface energy that is not the lowest of the three diasporite/corundum interfaces investigated here; at the same time, it was not found to have the highest interface energy either. It should be kept in mind that supercell 3 simulates only one of the many possible configurations of the diasporite(010)//corundum(11 $\bar{2}$ 0) interface. Unlike the interfaces simulated by the supercells here, real diasporite/corundum reaction interfaces are usually also not perfectly flat [\[16\]](#). Furthermore, dependent on experimental conditions, the dehydration of diasporite into corundum has not only been found to occur directly [\[65\]](#), but also *via* an intermediate diasporite-like [\[66\]](#) or corundum-like [\[67\]](#) transition phase. Only three, flat interface configurations were investigated in the present study, and interfaces with intermediate transition phases were not included at all. An investigation considering a larger number of interface configurations and including intermediate transition phases, might shed more light on the relationship between interface energy and the experimentally observed preferential direction of diasporite dehydration. Such a more extensive investigation is beyond the scope of the present study, however, but would be a most interesting follow-up study.

### 3.4. Interface charge effects

The results of the Bader charge analysis of the interface supercells

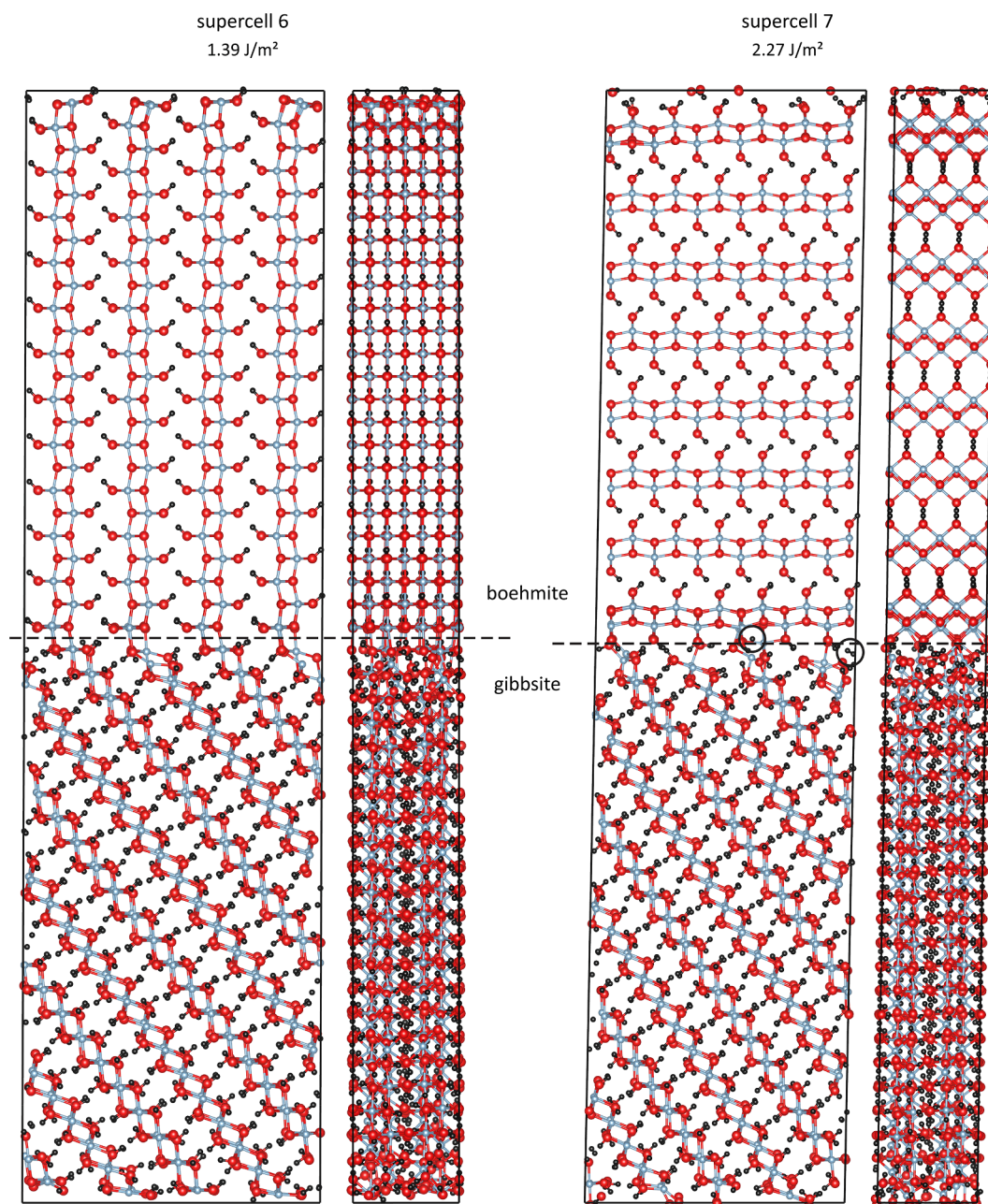


**Fig. 4.** The output configurations of supercells 6 and 7. For each supercell, the [100] (left) and [010] (right) projection are shown. The boundaries of the simulation cells are indicated with black solid lines. Dashed lines indicate the interfaces at  $Z_{\text{rel}} \approx 1/2$ . Light blue, red, and black spheres denote Al, O, and H atoms, respectively. Circled in black are, in supercell 7: one H interstitial, and one  $\text{H}_2$  molecule. Included are the values of the calculated interface energy. (For interpretation of the references to colour in this figure legend, the reader is referred to the web version of this article.)

can be found in Fig. 6, where the Bader charges of the atoms in the supercells are plotted as a function of the Z-coordinate (height) in the supercell (blue, red, and white circles). As can be seen from the comparison with Table 3, the atoms in supercells 1–3, 6, and 8, all have Bader charges that are very similar to the Bader charges of the atoms in the bulk phase unit cells. The same applies to the large majority of the atoms in supercells 4, 5, and 7. A number of atoms in the latter supercells, however, were found to show deviating values. These atoms were found to be part of dehydration-related defects such as chemisorbed  $\text{H}_2\text{O}$  and interstitial H, and will be discussed into more detail later.

Fig. 6 includes slab-wise summed charges for the supercells that were not found to contain interstitial dehydration defects after relaxation (black dots, with a dark grey line to guide the eye, over light blue vertical bars that indicate the thickness of the slabs). The slabs over which

the individual atomic Bader charges were summed to obtain the plotted values are all of stoichiometric composition. Surprisingly however, several slabs were found to have a nonzero summed charge. As can be seen from Fig. 6, this accumulation of positive or negative charge takes place near the interface and in supercells 1–3 and 8 results in the formation of interface dipoles. The same effect was observed in the supercells containing interstitial dehydration defects as well but is not shown here as, due to the dissociation of atoms from the constituting lattice and the migration of atoms in these supercells, the definition of stoichiometric slabs is not always possible here and the interpretation of summed-charge effects in slabs that are no longer stoichiometric and/or contain charged interstitial defects is beyond the scope of the present discussion.

For the definition of the stoichiometric slabs, different choices could

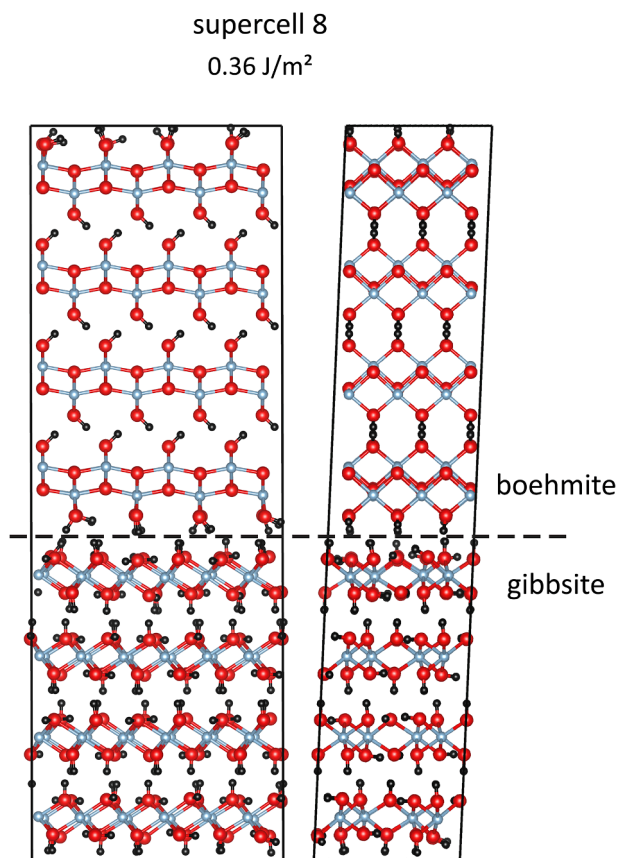


**Fig. 5.** The output configuration of supercell 8. On the left, the [100] projection is shown, and on the right, the [010] projection. Light blue, red, and black spheres denote Al, O, and H atoms, respectively. The boundaries of the simulation cell are indicated with black solid lines. The dashed line indicates the interface at  $Z_{\text{rel}} \approx 1/2$ . Included is the value of the calculated interface energy. (For interpretation of the references to colour in this figure legend, the reader is referred to the web version of this article.)

be made with regard to the slab boundaries. As the layered hydroxides considered in this study consist of single and double sheets of Al centered octahedra, the slabs in the supercells were chosen to be centered around Al-atomic planes. Planes of Al atoms with about the same  $Z$ -coordinate in the supercell will therefore be at the center of the slabs. The averaged  $Z$ -coordinate of these Al atoms defines the  $Z$ -coordinate of the slabs in Fig. 6. For supercells 2, 3, and 8, the definition of the slabs could be carried out in a most straightforward way. As can be seen from Fig. 5, supercell 8 in itself already exists of distinct layers parallel to the interface, and each of these layers defines one slab in the calculation of the slab-wise summed charges. In supercell 2, atoms that are at about the same height in the supercell are considered to form one slab (see also the [010] projection of this supercell in Fig. 2). The slabs in supercell 3 consist of Al layers that are sandwiched between two O layers or between one O layer and one OH layer (see also the [010] projection of this supercell in Fig. 2). The choice of the slab boundaries in supercell 1 is less straightforward. Different boundary definitions are possible here, and a different choice would change the picture, although it would still be showing charge accumulation at the interface, significantly. Here, in supercell 1, if an O atom connects Al atoms that are located in different slabs, its charge is in proportion assigned to each of these slabs; the charge of a H atom is assigned to the slab to which the O atom that it is connected to belongs. It should be noted that in contrast to the interface slabs in the other supercells, which all consist of only one bulk phase, the slabs at the interface in supercell 1 are in part corundum and in part diaspore (see also the [010] projection of this supercell in Fig. 2). For supercell 6, the boehmite component was most easily divided

into slabs by considering atoms that have about the same  $Z$ -coordinate to form one slab (see also the [100] projection of this supercell in Fig. 4). The atoms in the gibbsite component of supercell 6 were in principle assigned to slabs based on their height in the supercell as well, although reassignment by hand was sometimes needed here to preserve stoichiometry.

The observed accumulation of charge at the interfaces is the result of charge transfer across the interface. As can be seen from Fig. 6, the magnitude and direction of this charge transfer depends on the interface geometry. A possible explanation for the transfer of charge can be found from the structural analysis of the slabs. The slab thickness resulting from this analysis is included in Fig. 6, and as can be seen, slabs at the interface were found to have an increased or decreased slab thickness in comparison to the slabs located in the middle of the supercell bulk phase components. The Coulomb interactions of atoms near the interfaces include interactions of these atoms with atoms on the other side of the interface. As a result, these atoms are attracted or repelled in a way that differs from the attraction or repulsion that atoms further away from the interface experience from their Coulomb interactions with other atoms. This causes slabs near the interface to expand or contract, and this expansion and contraction comes at an energy cost. To reduce this energy penalty, small amounts of charge are transferred from one side of the interface to the other side of the interface. That this transfer of charge must be solely ascribed to polarization effects is unlikely, as the electrons of a polarized O atom are fully enclosed within the Bader volume of this atom and therefore the charge of these electrons is fully assigned to the O atom.

### 3.5. Interface dehydration defects

As mentioned earlier, the boehmite/ $\gamma$ -Al<sub>2</sub>O<sub>3</sub> interface in supercell 4 and the gibbsite/boehmite interfaces in supercells 5 and 7, were found to contain structural defects with atomic Bader charges that (sometimes very strongly) deviate from the perfect bulk values. These are defects that are related to the dehydration process. The present study is not a dynamic study. The results, however, show that these types of defects will in themselves already form at dehydration interfaces, *i.e.*, at the dehydration interfaces investigated here, and the observed separation of atoms from the constituting lattice and their subsequent migration through the lattice to form interstitial defects or reattach to the lattice during relaxation, may provide meaningful insights in the dehydration mechanism at the atomic level.

First the defects in the two gibbsite/boehmite configurations will be discussed, and then the defects in the boehmite/ $\gamma$ -Al<sub>2</sub>O<sub>3</sub> configuration. Interstitial defects that were already present in the initial input configuration, and defects that formed during relaxation from such defects, will not be discussed here. This is mainly the case for the interface configuration of supercell 7, which could not be constructed as defect-free as preferred, as otherwise the limit of computational feasibility of this study would be exceeded. Although in reality such defects will already be present in a sample and play a role in the dehydration process, here only the route of formation of interstitial defects that completely formed out of the bulk phase lattices will be discussed.

#### 3.5.1. Gibbsite $\rightarrow$ boehmite dehydration defects

Gibbsite knows various routes of dehydration (see also Fig. 1). Which transformation of gibbsite occurs, depends on the specific experimental conditions under which the dehydration takes place. Here, we are interested in the transformation of gibbsite into boehmite. The global picture is that this transformation only occurs in the presence of excess water vapor; in dry air, gibbsite transforms into  $\chi$ -Al<sub>2</sub>O<sub>3</sub>, and in vacuum, gibbsite transforms into  $\rho$ -Al<sub>2</sub>O<sub>3</sub> [1,2]. The precise reaction mechanism is unknown. There is a general consensus that the transformation of gibbsite into boehmite requires hydrothermal conditions in the crystal, where a water vapor overpressure is formed inside the crystallites and favors the formation of boehmite [68–70]. The mechanism, however, by

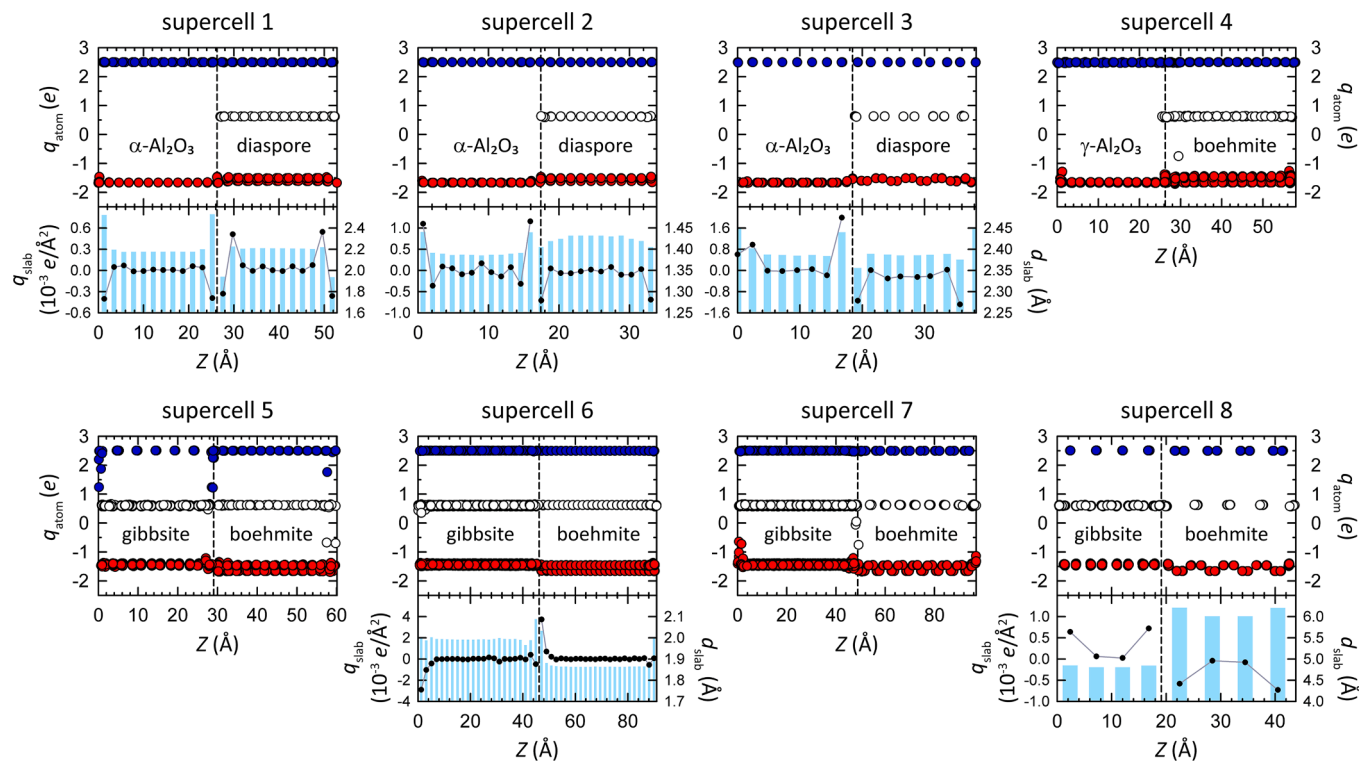


**Fig. 6.** Bader analysis results for the interface supercells. Blue, red, and white circles: atomic Bader charge ( $q_{\text{atom}}$ ) of Al, O, and H atoms, respectively, plotted as a function of the Z-coordinate in the supercell. Black dots: slab-wise summed Bader charge ( $q_{\text{slab}}$ ) of stoichiometric slabs, with scale bar on the left, and a dark grey line to guide the eye. Light blue vertical bars: thickness ( $d_{\text{slab}}$ ) of the stoichiometric slabs, with scale bar on the right. The vertical dashed line indicates the interface at  $Z_{\text{rel}} \approx 1/2$ . (For interpretation of the references to colour in this figure legend, the reader is referred to the web version of this article.)

which dehydration water is confined inside crystal grains to produce this overpressure, is still under debate. Explanations offered in the literature include the formation of an impervious layer around gibbsite particles resulting from the initial transformation of gibbsite at the surface into  $\gamma$ - $\text{Al}_2\text{O}_3$  or boehmite, after which water release from the particle is prevented and transformation into boehmite is favored (see, for example, the discussion in Naumann et al. [69], and references cited therein). Other models assume that the transformation of gibbsite into boehmite directly starts in the interior of the crystal, and that it is the gibbsite itself that, as a shell around the internally formed boehmite, slows down the release of water [68]. In both types of models, the formation of cracks, which can be experimentally observed, explains the generally detected sudden release of water vapor after a while. The migration of OH ions and  $\text{H}_2\text{O}$  molecules through the crystal lattice, which cannot be experimentally observed, is assumed to play a role in the release of water from the structure as well [68,69].

The formation of OH ions was not observed in the present study. Supercell 5, however, was found to contain two  $\text{H}_2\text{O}$  molecules after relaxation. These molecules followed a very similar route of formation. They are both located at the interface at  $Z_{\text{rel}} \approx 1/2$  (one is indicated in Fig. 3), and both were observed to form from two adjacent hydroxyl groups from the gibbsite lattice at that interface. During relaxation, the O atom of the OH group that was found to split off in its entirety to form the  $\text{H}_2\text{O}$  molecule and the H atom of the OH group that was found to split off only this H atom to form the  $\text{H}_2\text{O}$  molecule, first bent towards each other (Fig. 7a and b), trailing their OH-companion atom along. Subsequently, the OH group and the H atom separated from the lattice to form  $\text{H}_2\text{O}$  (Fig. 7c). After the separation, the Bader charge of the H atom remained a fairly unchanged (rounded) value of  $+0.6e$ , whereas the Bader charge of the O atom decreased to a (rounded) value of about  $-1.3e$ . The reduced charge of the O atom has the effect that the  $\text{H}_2\text{O}$  molecules, that are now interstitial to the gibbsite lattice, are nearly neutral or only very slightly charged; the summed-up Bader charges for

the molecules are  $-0.02e$  and  $-0.12e$ .

In addition to the two  $\text{H}_2\text{O}$  molecules, the interface at  $Z_{\text{rel}} \approx 1/2$  in supercell 5 was also found to contain two  $\text{OH}_2$  groups after relaxation (one is indicated in Fig. 3). These groups formed at the boehmite side of the interface. One resulted from the single detachment of an H atom from a hydroxyl group, and the subsequent reattachment of this H atom to the lattice after migration over a small distance along the interface, by bonding to a hydroxyl group, which as a consequence became an  $\text{OH}_2$  group. The other  $\text{OH}_2$  group in supercell 5 (encircled in Fig. 3) was found to be the result of a series of H transfers between hydroxyl groups by which in effect an H atom was transported away from the surface into the boehmite along the boehmite cleavage plane (Fig. 7e–h). Supercell 7 was found to contain one  $\text{OH}_2$  group that formed during relaxation as well. This group (not indicated in Fig. 4) is located at the gibbsite side of the interface at  $Z_{\text{rel}} \approx 1/2$ , and resulted from the single transfer of an H atom slightly away from the interface into the gibbsite. The Bader charges of the H and O atoms in the  $\text{OH}_2$  groups were all found to be similar to the Bader charges of the atoms in the  $\text{H}_2\text{O}$  molecules. The summed-up charges for the  $\text{OH}_2$  groups, following the order of their previous discussion, are  $-0.08e$ ,  $-0.12e$ , and  $-0.06e$ . In contrast to the  $\text{H}_2\text{O}$  molecules, which are interstitial to the lattice, the  $\text{OH}_2$  groups are clearly part of the lattice, with Al–O bond lengths ranging from 1.9 to 2.1 Å.

Both supercells 5 and 7 were also found to contain interstitial H after relaxation. Surprisingly, these H atoms were all found to have a negative Bader charge, of approximately  $-0.7e$ . In supercell 5 two of these electronegative ions formed, at the boehmite side of the interface at  $Z_{\text{rel}} \approx 0$ . In Fig. 3 these ions are located at the top of the supercell (one is indicated), and in Fig. 6 they are found at a high Z-coordinate value, as the interface at  $Z_{\text{rel}} \approx 0$  equals the interface at  $Z_{\text{rel}} \approx 1$  due to the periodic boundary conditions that apply to the calculations. In supercell 7 one interstitial H ion with a negative Bader charge formed, at the boehmite site of the interface at  $Z_{\text{rel}} \approx 1/2$  (encircled in Fig. 4). Hydride ions, *i.e.*,

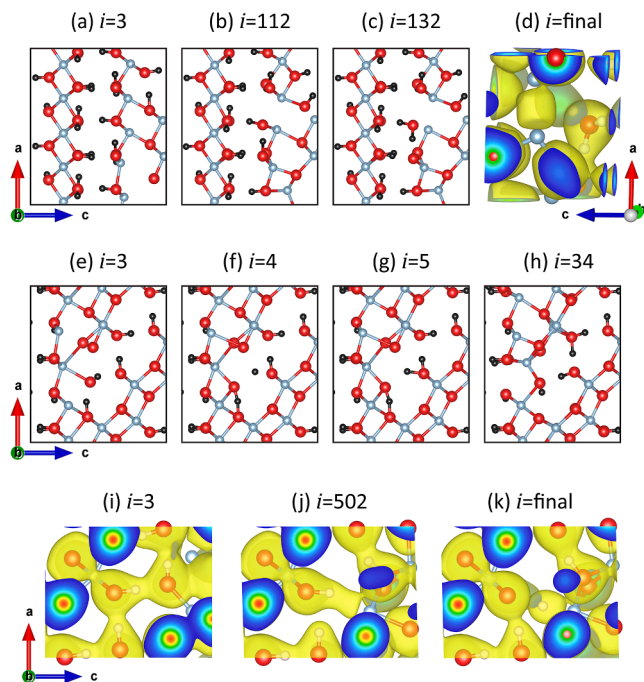


**Fig. 7.** Routes of defect formation during relaxation. All panels show [010] projections of sections of supercell 5 at various iteration steps  $i$ , except panel (d), which shows a  $\sim[0\bar{1}0]$  projection. The location of the defects in the supercell is indicated in Fig. 3. The atomic structural models in panels (a–c) show the formation of  $\text{H}_2\text{O}$  at the interface at  $Z_{\text{rel}} \approx 1/2$ . Panel (d) shows in further close-up the charge density around this molecule and the Al atoms from which it originated, as obtained after full relaxation; note that this panel shows a near- $180^\circ$  rotated view with respect to panels (a–c) to allow a better view of the charge density. The atomic structural models in panels (e–h) show the formation of  $\text{OH}_2$  groups at the interface at  $Z_{\text{rel}} \approx 1/2$  that are the result of multiple H transfers and by which in effect an H atom is transported away from the interface along the boehmite cleavage plane. The charge density plots in panels (i–k) show the formation of a hydride ion at the interface at  $Z_{\text{rel}} \approx 1$ . In the atomic structural models, light blue, red, and black spheres denote Al, O, and H atoms, respectively; in the charge density plots, H atoms are indicated by white spheres. All charge density plots show  $0.20 \text{ e}/\text{\AA}^3$  isosurfaces. (For interpretation of the references to colour in this figure legend, the reader is referred to the web version of this article.)

electronegative H ions with a valence state of  $-1$ , are known to exist, not only in, for example, metal hydrides, where hydrogen bonds to electropositive metal ions and assumes the formal  $\text{H}^-$  state, but also in metal oxides, where hydrogen is usually incorporated in the formal  $\text{H}^+$  state to form  $\text{OH}^-$  [71–73]. The negatively charged H atoms in supercells 5 and 7 are atoms that separated from OH groups, and are found in spaces interstitial to the lattice that are relatively large, as can most clearly be seen from Fig. 3 but is also the case in Fig. 4. Previous studies have shown that point-defect vacancies may trap, sometimes considerable amounts of charge [74]. The spaces in supercells 5 and 7 where after relaxation the electronegative H ions were found, trapped charge as well, during the initial stages of the relaxation, after which the H atoms split off and combined with the charge accumulated inside these spaces to obtain the formal  $\text{H}^-$  state. (In one case, in supercell 5, this separation is combined with a series of H transfers between hydroxyl groups.) A similar mechanism, where instead of one, two H atoms split off to combine with interstitially accumulated charge to obtain the formal  $\text{H}^0$  state, explains the formation of the neutral interstitial  $\text{H}_2$  molecule that was observed at the gibbsite site of the interface at  $Z_{\text{rel}} \approx 1/2$  in supercell 7 (encircled in Fig. 4). Bader charges for the H atoms in this molecule were found to be  $+0.05e$  and  $-0.06e$ .

As can be seen from Fig. 6, the Bader charge analysis of supercell 5 yielded values for Al atoms at and near the interface, that, sometimes

strongly deviate from calculated bulk values. Such deviations for Al atoms were not observed in any of the other supercells. It should be reminded that supercell 5, unlike the other supercells, was not built from an integer number of bulk phase unit cells, but that four Al atoms were added during construction of the simulation cell to ensure atomic coherency across the interfaces. The electrons introduced to the system by these extra atoms, that were added as neutral atoms but are electropositive in nature, are most likely the cause of the observed deviation. When performing Bader charge analysis to compute atomic charges, the boundary of an atom is defined by the zero flux-surface of the electron density and the charge contained within the volume enclosed by this surface is interpreted as the electronic charge of that atom. A closer inspection of the Bader analysis results revealed that for each of the Al atoms with a deviating Bader charge, the charge assigned to the atom is not so much located on the atom itself as it is near it. Fig. 7d illustrates this for two Al atoms at the interface at  $Z_{\text{rel}} \approx 1/2$ . Whereas Al atoms were generally found to be  $+2.5e$  Bader charged in all supercells, Bader analysis resulted in Bader charges of  $+1.2e$  and  $+2.3e$  for these two atoms. From Fig. 7d it can be clearly seen, however, how the excess charge density that resulted in these decreased values, is not centered around these two atoms but located between them. In this particular case, the presence of the charge is counterbalancing the absence of the OH group that previously bonded these two Al atoms (Fig. 7a) but migrated away to form  $\text{H}_2\text{O}$  (Fig. 7c). For the other deviating Al atoms, a similar presence of charge near the atom rather than on the atom was observed as well. The Bader algorithm assigned this charge as atomic charge to these atoms. Their resulting reduced Bader charge values, however, should not be understood as indicating reduced ionicity. They rather show that electronic charge accumulated in the vicinity of these Al atoms.

### 3.5.2. Boehmite $\rightarrow \gamma\text{-Al}_2\text{O}_3$ dehydration defects

Boehmite transforms into  $\gamma\text{-Al}_2\text{O}_3$  upon heating (see Fig. 1). The precise mechanism of this transformation is still unknown. In the experimental literature on the thermal decomposition of boehmite, two general types of mechanism have been suggested (see for a discussion, for example, Wilson [20], and references cited therein). One type models the mechanism as a process where  $\text{H}_2\text{O}$  is formed internally from protons and hydroxyl groups and then eliminated from the boehmite structure, after which Al cation redistribution causes the structure to collapse [19]. The other type involves counter migration of Al cations and protons, where protons diffuse away from between boehmite layers and create vacant interlayer sites that accommodate counterdiffusing Al cations; here, it is protons and hydroxyl groups near now-vacant Al sites that are the origin of the  $\text{H}_2\text{O}$  eliminated during dehydration [20].

A previous computational study by Krokidis et al. [15] assumed a model of the first type, and performed DFT and first-principles molecular dynamics simulations to investigate the thermal decomposition mechanism of boehmite. In that study, the jumping of H atoms between hydroxyl groups was observed, very much like the consecutive H transfers we observed between hydroxyl groups in the boehmite part of supercell 5, as described earlier and shown in Fig. 7e–h, and by which in effect an H atom was transported away through the boehmite cleavage plane. Those authors did not observe, however, the actual formation and release of  $\text{H}_2\text{O}$  from the boehmite structure during their simulations. From the boehmite/ $\gamma\text{-Al}_2\text{O}_3$  interface supercell (supercell 4), the formation of  $\text{H}_2\text{O}$  was not observed either, nor was any transfer of H between boehmite hydroxyl groups found. A negative H atom was found, however, at the boehmite side of the interface at  $Z_{\text{rel}} \approx 1/2$  and with a Bader charge of approximately  $-0.8e$ , whose formation occurred in a similar way as described above for the hydride ions in supercells 5 and 7. As can be seen from Fig. 3, the interface near this hydride ion showed a very strong restructuring during relaxation, where not only H atoms but also Al atoms displaced over quite long distances and the formation of a small, fully dehydrated boehmite patch was clearly observed. The interface configuration in supercell 4 was constructed most carefully

(see Fig. S2d), and it is very possible that the observed reconstruction indeed indicates boehmite dehydration at the investigated boehmite/ $\gamma$ - $\text{Al}_2\text{O}_3$  interface (just as the earlier described formation of  $\text{H}_2\text{O}$  molecules,  $\text{OH}_2$  groups, and H ions at interfaces indicate dehydration). The relaxation data, however, proved very difficult to be interpreted in terms of a dehydration mechanism. It is also very possible that the observed reconstruction indicates that, within the present boehmite and  $\gamma$ - $\text{Al}_2\text{O}_3$  phase orientation relationship, an interface with an orientation different from the currently investigated configuration is energetically more favorable. Further investigations are necessary to clarify this, but are beyond the limits of the present study.

#### 4. Conclusions

The results of a DFT study of aluminum hydrate dehydration interfaces using a van der Waals density functional have been presented. The interface configurations investigated here as a first exploration of possible diaspore/corundum, gibbsite/boehmite, and boehmite/ $\gamma$ - $\text{Al}_2\text{O}_3$  dehydration interface geometries, were all found to have a reasonable probability of occurring. Bader charge analysis revealed accumulation and transfer of small amounts of electronic charge across the interface to take place at all considered interfaces. In three supercells, the formation of dehydration-related interface defects during relaxation was observed. At the gibbsite side of gibbsite/boehmite interfaces, transfer of H atoms between hydroxyl groups and separation of hydroxyl groups and H atoms from the lattice, were observed to result in the formation of chemisorbed  $\text{H}_2\text{O}$  and  $\text{OH}_2$  groups. At the boehmite side, the formation of successive  $\text{OH}_2$  groups via a series of H transfers between hydroxyl groups was found to in effect transport an H atom away from the interface. Separation of H atoms from the lattice to form interstitial H was observed as well, in the boehmite part of both gibbsite/boehmite and boehmite/ $\gamma$ - $\text{Al}_2\text{O}_3$  interface simulation cells. In gibbsite, a similar separation of H atoms was found to lead to interstitial  $\text{H}_2$ . Accumulation of charge in spaces interstitial to the lattice was found to play a role in the formation of these defects.

The study of dehydration interfaces may be of added value when investigating the dehydration mechanism of hydrated alumina. The present study is an illustration of this, and offers various starting points for future studies. Both the gibbsite  $\rightarrow$  boehmite and boehmite  $\rightarrow$   $\gamma$ - $\text{Al}_2\text{O}_3$  transformation appear to be excellent candidates for dynamical first-principles follow-up studies. The prompt formation of  $\text{H}_2\text{O}$  in gibbsite observed here suggests that a pure-gibbsite simulation cell might suffice to observe the formation and release of  $\text{H}_2\text{O}$  from gibbsite during first-principles molecular dynamics simulations. For boehmite, on the other hand, given that from a previous first-principles molecular dynamics study using a pure-boehmite simulation cell the actual formation and release of  $\text{H}_2\text{O}$  from the structure could not be observed [15], whereas in the present study the full dehydration of a small patch of boehmite patch was observed to take place at the boehmite/ $\gamma$ - $\text{Al}_2\text{O}_3$  interface, the inclusion of such an interface in the starting configuration may be required to successfully observe the elimination of  $\text{H}_2\text{O}$  from boehmite during dynamical simulation. Another interesting topic of study are lattice defects and the role they play in the dehydration process, not only for gibbsite and boehmite, for which in the present study the accumulation of charge in vacancy-like spaces was found to play a role in the formation of dehydration-related defects, but for diaspore as well. A more elaborate study of possible diaspore  $\rightarrow$  corundum dehydration interface configurations, considering a larger number of possible interface geometries and including intermediate diaspore and corundum transition phases as well, might clarify the relationship between interface energy and the experimentally observed preferential direction of diaspore dehydration. Such a study would not necessarily require the use of DFT calculations, but could also be performed using classical molecular dynamics simulations (see for example Mei et al. [75], who used classical molecular dynamics simulations to study the interfacial layer between Al and corundum).

The present study shows the potential of interface studies for elucidating dehydration pathways and the role that defects play in the associated transformations. Its outcomes can be used as starting-points for various follow-up studies, of which a few were pointed out above. The dehydration processes of the various aluminum hydrates are complex and multi-stage processes that cannot be studied using DFT alone. Follow-up studies should therefore not be limited to DFT studies, but include molecular dynamics, Monte Carlo, phase-field, and other continuum methods as well, and incorporate models that take the external chemical and physical environment into account, preferably in a multi-scale approach. Combined they will help to further unravel the mechanism of dehydration of the aluminum hydrates investigated here, and together with previous and future computational and experimental studies one day maybe even lead to a complete understanding of the transformation mechanisms at the atomic level.

#### Declaration of Competing Interest

The author declares that she has no known competing financial interests or personal relationships that could have appeared to influence the work reported in this paper.

#### Acknowledgements

This work was carried out on the Dutch national e-infrastructure with the support of SURF Cooperative and NWO Reken tijd (Grant No. 15225). Figures of atomic structural models and charge density plots were produced using VESTA [78]. Table 2 includes bulk phase lattice parameters from a previous simulation study [28] that were kindly provided upon request by A. R. Ferreira, lead author of that study.

#### Appendix A. Supplementary data

Supplementary data to this article can be found online at <https://doi.org/10.1016/j.apsusc.2020.148501>.

#### References

- [1] C.V. Chandran, C.E.A. Kirschhock, S. Radhakrishnan, F. Taulelle, J.A. Martens, E. Breynaert, Alumina: discriminative analysis using 3D correlation of solid-state NMR parameters, *Chem. Soc. Rev.* 48 (2019) 134–156, <https://doi.org/10.1039/c8cs00321a>.
- [2] G. Busca, Structural, surface, and catalytic properties of aluminas, *Adv. Catal.* 57 (2014) 319–404, <https://doi.org/10.1016/B978-0-12-800127-1.00003-5>.
- [3] K. Wefers, C. Misra, Oxides and hydroxides of aluminum, Alcoa Technical Paper No. 19, revised, Alcoa Laboratories, Pittsburgh, PA, 1987.
- [4] J.M. McHale, A. Auroux, A.J. Perrotta, A. Navrotsky, Surface energies and thermodynamic phase stability in nanocrystalline aluminas, *Science* 277 (1997) 788–791, <https://doi.org/10.1126/science.277.5327.788>.
- [5] L. Liao, J. Bai, Y. Qu, Y.-C. Lin, Y. Li, Y. Huang, X. Duan, High- $\kappa$  oxide nanoribbons as gate dielectrics for high mobility top-gated graphene transistors, *Proc. Natl. Acad. Sci. USA* 107 (2010) 6711–6715, <https://doi.org/10.1073/pnas.0914117107>.
- [6] S.H. Chae, W.J. Yu, J.J. Bae, D.L. Duong, D. Perello, H.Y. Jeong, Q.H. Ta, T.H. Ly, Q.A. Vu, M. Yun, X. Duan, Y.H. Lee, Transferred wrinkled  $\text{Al}_2\text{O}_3$  for highly stretchable and transparent graphene-carbon nanotube transistors, *Nat. Mater.* 12 (2013) 403–409, <https://doi.org/10.1038/NMAT3572>.
- [7] M.W. Jung, W. Song, W.J. Choi, D.S. Jung, Y.J. Chung, S. Myung, S.S. Lee, J. Lim, C.-Y. Park, J.-O. Lee, K.-S. An, Fabrication of free-standing  $\text{Al}_2\text{O}_3$  nanosheets for high mobility flexible graphene field effect transistors, *J. Mater. Chem. C* 2 (2014) 4759–4763, <https://doi.org/10.1039/c4tc00041b>.
- [8] X. Zhang, P.L. Huestis, C.I. Pearce, J.Z. Hu, K. Page, L.M. Anovitz, A. B. Aleksandrov, M.P. Prange, S. Kerisit, M.E. Bowden, W. Cui, Z. Wang, N. R. Jaegers, T.R. Graham, M. Dembowski, H.-W. Wang, J. Liu, A.T. N'Diaye, M. Bleuel, D.F.R. Mildner, T.M. Orlando, G.A. Kimmel, J.A. La Verne, S.B. Clark, K. M. Rosso, Boehmite and gibbsite nanoplates for the synthesis of advanced alumina products, *ACS Appl. Nano Mater.* 1 (2018) 7115–7128, <https://doi.org/10.1021/acsnano.8b01969>.
- [9] A. Zavabeti, B.Y. Zhang, I.A. de Castro, J.Z. Ou, B.J. Carey, M. Mohiuddin, R. S. Datta, C. Xu, A.P. Mouritz, C.F. McConville, A.P. O'Mullane, T. Daeneke, K. Kalantar-Zadeh, Green synthesis of low-dimensional aluminum oxide hydroxide and oxide using liquid metal reaction media: Ultrahigh flux membranes, *Adv. Funct. Mater.* 28 (2018) 1804057, <https://doi.org/10.1002/adfm.201804057>.

- [10] T.E. Bell, J.M. González-Carballo, R.P. Toozé, L. Torrente-Murciano, Single-step synthesis of nanostructured  $\gamma$ -alumina with solvent reusability to maximise yield and morphological purity, *J. Mater. Chem. A* 3 (2015) 6196–6201, <https://doi.org/10.1039/c4ta06692h>.
- [11] T.E. Bell, J.M. González-Carballo, R.P. Toozé, L. Torrente-Murciano,  $\gamma$ -Al<sub>2</sub>O<sub>3</sub> nanorods with tuneable dimensions – a mechanistic understanding of their hydrothermal synthesis, *RSC Adv.* 7 (2017) 22369–22377, <https://doi.org/10.1039/c7ra02590d>.
- [12] R. Demichelis, Y. Noël, P. Ugliengo, C.M. Zicovich-Wilson, R. Dovesi, Physico-chemical features of aluminum hydroxides as modeled with the hybrid B3LYP functional and localized basis functions, *J. Phys. Chem. C* 115 (2011) 13107–13134, <https://doi.org/10.1021/jp200523x>.
- [13] M.F. Peintinger, M.J. Kratz, T. Bredow, Quantum-chemical study of stable, metastable and high-pressure alumina polymorphs and aluminum hydroxides, *J. Mater. Chem. A* 2 (2014) 13143–13158, <https://doi.org/10.1039/c4ta02663b>.
- [14] S. Nagendran, G. Periyasamy, P.V. Kamath, DFT study of polymorphism in Al(OH)<sub>3</sub>: A structural synthon approach, *Z. Anorg. Allg. Chem.* 641 (2015) 2396–2403, <https://doi.org/10.1002/zaac.201500226>.
- [15] X. Krokidis, P. Raybaud, A.-E. Gobichon, B. Rebours, P. Euzen, H. Toulhoat, Theoretical study of the dehydration process of boehmite to  $\gamma$ -alumina, *J. Phys. Chem. B* 105 (2001) 5121–5130, <https://doi.org/10.1021/jp0038310>.
- [16] L. Löffler, W. Mader, Electron microscopic study of the dehydration of diasporite, *Am. Mineral.* 86 (2001) 293–303, <https://doi.org/10.2138/am-2001-2-312>.
- [17] M. Dion, H. Rydberg, E. Schröder, D.C. Langreth, B.I. Lundqvist, Van der Waals density functional for general geometries, *Phys. Rev. Lett.* 92 (2004) 246401, <https://doi.org/10.1103/PhysRevLett.92.246401>.
- [18] J. Klimeš, D.R. Bowler, A. Michaelides, Chemical accuracy for the van der Waals density functional, *J. Phys.: Cond. Matt.* 22 (2010) 022201, <https://doi.org/10.1088/0953-8984/22/2/022201>.
- [19] H. Saalfeld, The dehydration of gibbsite and the structure of a tetragonal  $\gamma$ -Al<sub>2</sub>O<sub>3</sub>, *Clay Min. Bull.* 3 (1958) 249–257.
- [20] S.J. Wilson, The dehydration of boehmite,  $\gamma$ -AlOOH, to  $\gamma$ -Al<sub>2</sub>O<sub>3</sub>, *J. Solid State Chem.* 30 (1979) 247–255, [https://doi.org/10.1016/0022-4596\(79\)90106-3](https://doi.org/10.1016/0022-4596(79)90106-3).
- [21] S.R. Egorova, A.N. Mukhamedyarova, A.A. Lamberov, Specific features of the phase transition of gibbsite into boehmite under hydrothermal treatment of floccules in an aqueous suspension, *Russ. J. Appl. Chem.* 88 (2015) 758–768, <https://doi.org/10.1134/S1070427215050079>.
- [22] R.F.W. Bader, *Atoms in Molecules: A Quantum Theory*, Oxford University Press, Oxford, U.K., 1990.
- [23] I. Levin, D. Brandon, Metastable alumina polymorphs: Crystal structures and transition sequences, *J. Am. Ceram. Soc.* 81 (1998) 1995–2012, <https://doi.org/10.1111/j.1151-2916.1998.tb02581.x>.
- [24] R.J. Hill, Crystal structure refinement and electron density distribution in diasporite, *Phys. Chem. Miner.* 5 (1979) 179–200, <https://doi.org/10.1007/BF00307552>.
- [25] H. Saalfeld, M. Wedde, Refinement of the crystal structure of gibbsite Al(OH)<sub>3</sub>, *Z. Kristallogr.* 139 (1974) 129–135, <https://doi.org/10.1524/zkri.1974.139.1-2.129>.
- [26] H.O. Ayoola, S.D. House, C.S. Bonifacio, K. Kisslinger, W.A. Saidi, J.C. Yang, Evaluating the accuracy of common  $\gamma$ -Al<sub>2</sub>O<sub>3</sub> structure models by selected area electron diffraction from high-quality crystalline  $\gamma$ -Al<sub>2</sub>O<sub>3</sub>, *Acta Mater.* 182 (2020) 257–266, <https://doi.org/10.1016/j.actamat.2019.10.027>.
- [27] G. Paglia, A.L. Rohl, C.E. Buckley, J.D. Gale, Determination of the structure of  $\gamma$ -alumina from interatomic potential and first-principles calculations: The requirement of significant numbers of nonspinel positions to achieve an accurate structural model, *Phys. Rev. B* 71 (2005) 224115, <https://doi.org/10.1103/PhysRevB.71.224115>.
- [28] A.R. Ferreira, E. Küçükbenli, A.A. Leitão, S. de Gironcoli, *Ab initio* <sup>27</sup>Al NMR chemical shifts and quadrupolar parameters for Al<sub>2</sub>O<sub>3</sub> phases and their precursors, *Phys. Rev. B* 84 (2011) 235119, <https://doi.org/10.1103/PhysRevB.84.235119>.
- [29] Y. Rozita, R. Brydson, T.P. Comyn, A.J. Scott, C. Hammond, A. Brown, S. Chauruka, A. Hassanpour, N.P. Young, A.I. Kirkland, H. Sawada, R.I. Smith, A study of commercial nanoparticulate  $\gamma$ -Al<sub>2</sub>O<sub>3</sub> catalyst supports, *ChemCatChem* 5 (2013) 2695–2706, <https://doi.org/10.1002/cctc.201200880>.
- [30] L. Samain, A. Jaworski, M. Edén, D.M. Ladd, D.-K. Seo, F.J. Garcia-Garcia, U. Häussermann, Structural analysis of highly porous  $\gamma$ -Al<sub>2</sub>O<sub>3</sub>, *J. Solid State Chem.* 217 (2014) 1–8, <https://doi.org/10.1016/j.jssc.2014.05.004>.
- [31] G. Paglia, C.E. Buckley, A.L. Rohl, B.A. Hunter, R.D. Hart, J.V. Hanna, L.T. Byrne, Tetragonal structure model for boehmite-derived  $\gamma$ -alumina, *Phys. Rev. B* 68 (2003) 144110, <https://doi.org/10.1103/PhysRevB.68.144110>.
- [32] G. Paglia, E.S. Božin, S.J.L. Billinge, Fine-scale nanostructure in  $\gamma$ -Al<sub>2</sub>O<sub>3</sub>, *Chem. Mater.* 18 (2006) 3242–3248, <https://doi.org/10.1021/cm060277j>.
- [33] M. Digne, P. Sautet, P. Raybaud, P. Euzen, H. Toulhoat, Use of DFT to achieve a rational understanding of acid–base properties of  $\gamma$ -alumina surfaces, *J. Catal.* 226 (2004) 54–68, <https://doi.org/10.1016/j.jcat.2004.04.020>.
- [34] G. Kresse, J. Hafner, *Ab initio* molecular-dynamics simulation of the liquid-metal-amorphous-semiconductor transition in germanium, *Phys. Rev. B* 49 (1994) 14251–14269, <https://doi.org/10.1103/PhysRevB.49.14251>.
- [35] G. Kresse, J. Furthmüller, Efficiency of *ab-initio* total energy calculations for metals and semiconductors using a plane-wave basis set, *Comput. Mater. Sci.* 6 (1996) 15–50, [https://doi.org/10.1016/0927-0256\(96\)00008-0](https://doi.org/10.1016/0927-0256(96)00008-0).
- [36] G. Kresse, J. Furthmüller, Efficient iterative schemes for *ab initio* total-energy calculations using a plane-wave basis set, *Phys. Rev. B* 54 (1996) 11169, <https://doi.org/10.1103/PhysRevB.54.11169>.
- [37] P.E. Blöchl, Projector augmented-wave method, *Phys. Rev. B* 50 (1994) 17953–17979, <https://doi.org/10.1103/PhysRevB.50.17953>.
- [38] G. Kresse, D. Joubert, From ultrasoft pseudopotentials to the projector augmented-wave method, *Phys. Rev. B* 59 (1999) 1758–1775, <https://doi.org/10.1103/PhysRevB.59.1758>.
- [39] J.P. Perdew, K. Burke, M. Ernzerhof, Generalized gradient approximation made simple, *Phys. Rev. Lett.* 77 (1996) 3865–3868, <https://doi.org/10.1103/PhysRevLett.77.3865>.
- [40] R. Demichelis, B. Civalleri, P. D'Arco, R. Dovesi, Performance of 12 DFT functionals in the study of crystal systems: Al<sub>2</sub>SiO<sub>5</sub> orthosilicates and Al hydroxides as a case study, *Int. J. Quantum Chem.* 110 (2010) 2260–2273, <https://doi.org/10.1002/qua.22574>.
- [41] J. Klimeš, D.R. Bowler, A. Michaelides, Van der Waals density functionals applied to solids, *Phys. Rev. B* 83 (2011) 195131, <https://doi.org/10.1103/PhysRevB.83.195131>.
- [42] C. Zhang, J. Wu, G. Galli, F. Gygi, Structural and vibrational properties of liquid water from van der Waals density functionals, *J. Chem. Theory Comput.* 7 (2011) 3054–3061, <https://doi.org/10.1021/ct200329e>.
- [43] G. Graziano, J. Klimeš, F. Fernandez-Alonso, A. Michaelides, Improved description of soft layered materials with van der Waals density functional theory, *J. Phys.: Condens. Matter* 24 (2012) 424216, <https://doi.org/10.1088/0953-8984/24/42/424216>.
- [44] F. Tran, J. Hutter, Nonlocal van der Waals functionals: The case of rare-gas dimers and solids, *J. Chem. Phys.* 138 (2013) 204103, <https://doi.org/10.1063/1.4807332>.
- [45] C.M. Fang, W.-F. Li, R.S. Koster, J. Klimeš, A. van Blaaderen, M.A. van Huis, The accurate calculation of the band gap of liquid water by means of GW corrections applied to plane-wave density functional theory molecular dynamics simulations, *Phys. Chem. Chem. Phys.* 17 (2015) 365, <https://doi.org/10.1039/c4cp04202f>.
- [46] S. Grimme, J. Antony, S. Ehrlich, H. Krieg, A consistent and accurate *ab initio* parametrization of density functional dispersion correction (DFT-D) for the 94 elements H–Pu, *J. Chem. Phys.* 132 (2010) 154104, <https://doi.org/10.1063/1.3382344>.
- [47] A.V. Krukau, O.A. Vydrov, A.F. Izmaylov, G.E. Scuseria, Influence of the exchange screening parameter on the performance of screened hybrid functionals, *J. Chem. Phys.* 125 (2006) 224106, <https://doi.org/10.1063/1.2404663>.
- [48] H.J. Monkhorst, J.D. Pack, Special points for Brillouin-zone integrations, *Phys. Rev. B* 13 (1976) 5188–5192, <https://doi.org/10.1103/PhysRevB.13.5188>.
- [49] G. Henkelman, A. Arnaldsson, H. Jónsson, A fast and robust algorithm for Bader decomposition of charge density, *Comput. Mater. Sci.* 36 (2006) 254–360, <https://doi.org/10.1016/j.commatsci.2005.04.010>.
- [50] E. Sanville, S.D. Kenny, R. Smith, G. Henkelman, Improved grid-based algorithm for Bader charge allocation, *J. Comput. Chem.* 28 (2007) 899–908, <https://doi.org/10.1002/jcc.20575>.
- [51] W. Tang, E. Sanville, G. Henkelman, A grid-based Bader analysis algorithm without lattice bias, *J. Phys.: Condens. Matter* 21 (2009) 084204, <https://doi.org/10.1088/0953-8984/21/8/084204>.
- [52] A. Platonenko, S. Piskunov, Y.F. Zhukovskii, E.A. Kotomin, *Ab initio* simulations on Frenkel pairs of radiation defects in corundum, *IOP Conf. Ser. Mater. Sci.* 77 (2015) 012001, <https://doi.org/10.1088/1757-899X/77/1/012001>.
- [53] J.C. Conesa, The relevance of dispersion interactions for the stability of oxide phases, *J. Phys. Chem. C* 114 (2010) 22718–22726, <https://doi.org/10.1021/jp109105g>.
- [54] J. Olivier, R. Poirier, Electronic structure of Al<sub>2</sub>O<sub>3</sub> from electron energy loss spectroscopy, *Surf. Sci.* 105 (1981) 347–356, [https://doi.org/10.1016/0039-6028\(81\)90167-9](https://doi.org/10.1016/0039-6028(81)90167-9).
- [55] R.H. French, Electronic band structure of Al<sub>2</sub>O<sub>3</sub>, with comparison to AlON and AlN, *J. Am. Ceram. Soc.* 73 (1990) 477–489, <https://doi.org/10.1111/j.1151-2916.1990.tb06541.x>.
- [56] E.O. Filatova, A.S. Konashuk, Interpretation of the changing the band gap of Al<sub>2</sub>O<sub>3</sub> depending on its crystalline form: connection with different local symmetries, *J. Phys. Chem. C* 119 (2015) 20755–20761, <https://doi.org/10.1021/acs.jpcc.5b06843>.
- [57] B. Ealet, M.H. Elyakhlofi, E. Gillet, M. Ricci, Electronic and crystallographic structure of  $\gamma$ -alumina thin films, *Thin Solid Films* 250 (1994) 92–100, [https://doi.org/10.1016/0040-6090\(94\)90171-6](https://doi.org/10.1016/0040-6090(94)90171-6).
- [58] M.P. Prange, X. Zhang, E.S. Ilton, L. Kovarik, M.H. Engelhard, S.N. Kerisit, Electronic response of aluminum-bearing minerals, *J. Chem. Phys.* 149 (2018) 024502, <https://doi.org/10.1063/1.5037104>.
- [59] L.H. Liang, X.M. You, H.S. Ma, Y.G. Wei, Interface energy and its influence on interface fracture between metal and ceramic thin films in nanoscale, *J. Appl. Phys.* 108 (2010) 084317, <https://doi.org/10.1063/1.3501090>.
- [60] M. Asta, S.M. Foiles, A.A. Quong, First-principles calculations of bulk and interfacial thermodynamic properties for fcc-based Al–Sc alloys, *Phys. Rev. B* 57 (1998) 11265–11275, <https://doi.org/10.1103/PhysRevB.57.11265>.
- [61] A. Costa e Silva, J. Ágren, M.T. Clavaguera-Mora, D. Djurovic, T. Gomez-Acebo, B.-J. Lee, Z.-K. Liu, P. Miodownik, H.J. Seifert, Applications of computational thermodynamics—the extension from phase equilibrium to phase transformations and other properties, *CALPHAD* 31 (2007) 53–74, <https://doi.org/10.1016/j.calphad.2006.02.006>.
- [62] Y. Wang, Z.-K. Liu, L.-Q. Chen, C. Wolverton, First-principles calculations of  $\beta''$ -Mg<sub>2</sub>Si<sub>6</sub>/ $\alpha$ -Al interfaces, *Acta Mater.* 55 (2007) 5934–5947, <https://doi.org/10.1016/j.actamat.2007.06.045>.
- [63] Y. Tu, J. Tersoff, Structure and energetics of the Si–SiO<sub>2</sub> interface, *Phys. Rev. Lett.* 84 (2000) 4393–4396, <https://doi.org/10.1103/PhysRevLett.84.4393>.
- [64] K.T. Butler, G. Sai Gautam, P. Canepa, Designing interfaces in energy materials applications with first-principles calculations, *npj Comput. Mater.* 5 (2019) 19, <https://doi.org/10.1038/s41524-019-0160-9>.

- [65] T. Tsuchida, K. Horigome, The effect of grinding on the thermal decomposition of alumina monohydrates,  $\alpha$ - and  $\beta$ - $\text{Al}_2\text{O}_3 \cdot \text{H}_2\text{O}$ , *Thermochim. Acta* 254 (1995) 359–370, [https://doi.org/10.1016/0040-6031\(94\)02052-P](https://doi.org/10.1016/0040-6031(94)02052-P).
- [66] L. Löffler, W. Mader, Transformation mechanism of the dehydration of diaspore, *J. Am. Ceram. Soc.* 86 (2003) 534–540, <https://doi.org/10.1111/j.1151-2916.2003.tb03337.x>.
- [67] A.H. Carim, G.S. Rohrer, N.R. Dando, S.-Y. Tzeng, C.L. Rohrer, A.J. Perrotta, Conversion of diaspore to corundum: a new  $\alpha$ -alumina transformation sequence, *J. Am. Ceram. Soc.* 80 (1997) 2677–2680, <https://doi.org/10.1111/j.1151-2916.1997.tb03171.x>.
- [68] J. Rouquerol, F. Rouquerol, M. Ganteaume, Thermal decomposition of gibbsite under low pressures. I. Formation of the boehmitic phase, *J. Catal.* 36 (1975) 99–110, [https://doi.org/10.1016/0021-9517\(75\)90014-7](https://doi.org/10.1016/0021-9517(75)90014-7).
- [69] R. Naumann, K. Köhnke, J. Paulik, F. Paulik, Kinetics and mechanism of the dehydration of hydrargillites. Part II, *Thermochim. Acta* 64 (1983) 15–26, [https://doi.org/10.1016/0040-6031\(83\)80124-5](https://doi.org/10.1016/0040-6031(83)80124-5).
- [70] J.M. Rivas Mercury, P. Pena, A.H. de Aza, D. Sheptyakov, X. Turrillas, On the decomposition of synthetic gibbsite studied by neutron thermodiffraction, *J. Am. Ceram. Soc.* 89 (2006) 3728–3733, <https://doi.org/10.1111/j.1551-2916.2006.01191.x>.
- [71] T. Norby, M. Widerøe, R. Glöckner, Y. Larring, Hydrogen in oxides, *Dalton Trans.* 19 (2004) 3012–3018, <https://doi.org/10.1039/B403011G>.
- [72] M. Widerøe, N. Kochetova, T. Norby, Transport numbers from hydrogen concentration cells over different oxides under oxidising and reducing conditions, *Dalton Trans.* 19 (2004) 3147–3151, <https://doi.org/10.1039/B402824D>.
- [73] K. Hayashi, P.V. Sushko, Y. Hashimoto, A.L. Shluger, H. Hosono, Hydride ions in oxide hosts hidden by hydroxide ions, *Nat. Commun.* 5 (2014) 3515, <https://doi.org/10.1038/ncomms4515>.
- [74] H. van Gog, M.A. van Huis, Structural and electronic properties of Frenkel and Schottky defects at the  $\text{MgO}\{100\}$  surface: spin polarization, mid-band gap states, and charge trapping at vacancy sites, *J. Phys. Chem. C* 123 (2019) 14408–14420, <https://doi.org/10.1021/acs.jpcc.9b01908>.
- [75] H. Mei, Q. Liu, L. Liu, X. Lai, W. She, P. Zhai, Molecular dynamics simulations of the microstructure of the aluminum/alumina interfacial layer, *Appl. Surf. Sci.* 324 (2015) 538–546, <https://doi.org/10.1016/j.apsusc.2014.10.138>.
- [76] L. Lutterotti, P. Scardi, Simultaneous structure and size-strain refinement by the Rietveld method, *J. Appl. Cryst.* 23 (1990) 246–252, <https://doi.org/10.1107/S0021889890002382>.
- [77] A.N. Christensen, M.S. Lehmann, P. Convert, Deuteration of crystalline hydroxides. Hydrogen bonds of  $\gamma$ - $\text{AlOO}(\text{H}, \text{D})$  and  $\gamma$ - $\text{FeOO}(\text{H}, \text{D})$ , *Acta Chem. Scand.* 36 (1982) 303–308, <https://doi.org/10.3891/acta.chem.scand.36a-0303>.
- [78] K. Momma, F. Izumi, VESTA 3 for three-dimensional visualization of crystal, volumetric and morphology data, *J. Appl. Crystallogr.* 44 (2011) 1272–1276, <https://doi.org/10.1107/S0021889811038970>.